RICE UNIVERSITY

Computational Simulation of Secondary Organic Aerosol (SOA) Formation from Toluene Oxidation

by

Ying Liu

A THESIS SUBMITTED
IN PARTIAL FULFILLMENT OF THE
REQUIREMENTS FOR THE DEGREE

Master of Science

APPROVED, THESIS COMMITTEE:

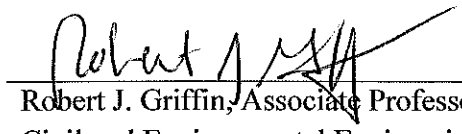

Robert J. Griffin, Associate Professor, Department of Civil and Environmental Engineering

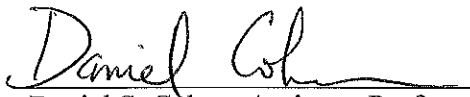

Daniel S. Cohan, Assistant Professor, Department of Civil and Environmental Engineering

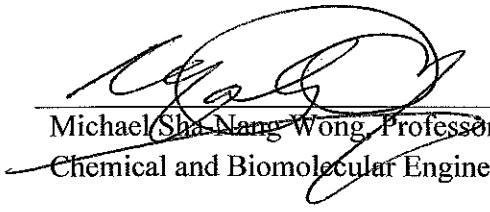

Michael Sha-Nang Wong, Professor, Department of Chemical and Biomolecular Engineering

HOUSTON, TEXAS
MAY 2012

RICE UNIVERSITY

Computational Simulation of Secondary Organic Aerosol (SOA) Formation from Toluene Oxidation

by

Ying Liu

A THESIS SUBMITTED
IN PARTIAL FULFILLMENT OF THE
REQUIREMENTS FOR THE DEGREE

Master of Science

APPROVED, THESIS COMMITTEE:

Robert J. Griffin, Associate Professor, Department of Civil and Environmental Engineering

Daniel S. Cohan, Assistant Professor, Department of Civil and Environmental Engineering

Michael Sha-Nang Wong, Professor, Department of Chemical and Biomolecular Engineering

HOUSTON, TEXAS
MAY 2012

ABSTRACT

Computational Simulation of Secondary Organic Aerosol (SOA) Formation

from Toluene Oxidation

by

Ying Liu

Toluene is one of the most prevalent aromatic volatile organic compounds (VOCs) in the atmosphere and has large secondary organic aerosol (SOA) yields compared to many other aromatic VOCs. Recent photo-oxidation studies highlight that toluene oxidation produces more SOA than observed previously, particularly at low levels of nitrogen oxides (NO_x). This study focuses on: 1.) the development of a gas-phase chemical mechanism describing toluene oxidation by hydroxyl radicals (OH); 2.) the prediction of SOA formation from toluene oxidation products; and 3.) the impact of NO_x level on SOA formation. The oxidation mechanism, which includes multiple pathways after the initial OH attack, has been incorporated into the Caltech Atmospheric Chemistry Mechanism (CACM). Toluene concentrations simulated in chamber experiments by the updated CACM as a function of time are typically within 5% of observed values for most experiments. Predicted ozone and NO_2 concentrations are typically within 15% of the experimental values. The gas-phase mechanism indicates the importance of bicyclic peroxy radical reactions in determining the product distribution and thus the likelihood of SOA formation. A gas-aerosol partitioning model is used in conjunction with the gas-phase mechanism to simulate SOA formation. Predicted SOA concentrations are typically within 15% of the experimental values. Under low NO_x conditions, simulation shows that more than 98% of SOA mass is contributed by bicyclic products from reactions between bicyclic peroxy radicals and other peroxy radicals. Increasing NO_x levels cause bicyclic peroxy radicals to react with NO

or nitrate radical, leading to fragmentation products that are less likely to form SOA. SOA yield dropped from 19.26% with zero initial NO_x to 13.27% with 100 ppb initial NO because of the change in the amount of toluene consumed. Composition of NO_x also has an impact on SOA yield and formation, showing that NO has a greater impact on SOA yield and formation than NO_2.

Acknowledgements

This work has been funded through National Science Foundation project ATM 0901580. The author would like to thank Dr. Griffin for advising the whole project and providing great support. The author would also like to thank Dr. David Cocker and his group for providing experimental data and advice on the toluene oxidation mechanism and Dr. Donald Dabdub for providing the platform to run the models and helping with modeling techniques.

Table of Contents

List of Tables and Figures

1. Introduction

Fine particle pollution is a key environmental concern and has important impacts, including in climate forcing, in negative health effects, and in poor visibility (Charlson et al., 1992; Lee and Sequeira, 1998; Schwartz and Neas, 2000). Secondary organic aerosol (SOA) is a significant component of rural and urban fine particulate matter and is generated in one particular pathway from condensation and/or nucleation of the oxidation products of volatile organic compounds (VOC) in the atmosphere (e.g., Volkamer et al., 2006). Toluene ($C_6H_5CH_3$), mainly related to fuel combustion in automobiles, is one of the most significant contributors to aromatic VOC in the atmosphere (Chan et al., 1991; Na et al., 2005). Toluene reacts primarily with hydroxyl radical (OH) in the atmosphere and produces more SOA per mass reacted (yield) than other aromatic VOC (Pandis et al., 1992). Furthermore, the SOA mass concentration produced from photo-oxidation of toluene has been observed recently to be larger than that observed by earlier studies, particularly with respect to its dependence on atmospheric oxides of nitrogen (NO_x: NO and NO_2) (Ng et al., 2007). Experiments conducted by Ng et al. (2007) proved that SOA yields from toluene oxidation under low-NO_x conditions were much larger than those under high-NO_x conditions. Previous laboratory studies and computational simulations (Stroud et al., 2004; Hu et al., 2007; Sato et al., 2007) also suggest the existence of a complicated mechanism of toluene oxidation in the atmosphere.

The most recent studies focusing on SOA formation simulation from toluene oxidation include Cao and Jang (2010) and Kamens et al. (2011). Cao and Jang (2010) applied toluene reactions from the fully explicit Master Chemical Mechanism (MCM) version 3.1 directly (Jenkin et al., 2003). The resulting products were used to predict SOA formation in a partitioning model that includes semi-empirical heterogeneous reactions. The experimental data

were obtained through experiments conducted in a 2-m^3 indoor Teflon®-film chamber, in the presence of inorganic aerosol seeds, and under various NO_x and humidity levels. It was shown that toluene decay was too slow in MCM simulations (Cao and Jang, 2010) but that the SOA simulations were within ± 15% of experimental results. However, due to the lack of experimental information on heterogeneous reactions, many parameters that were not validated were used. Kamens et al. (2011), on the other hand, adopted a completely differently approach to develop a condensed gas-phase chemistry for toluene oxidation based on the aromatic summary presented by Calvert et al. (2002). The partitioning model proposed two major particle formation mechanisms: 1. Gas-phase glyoxal and methylglyoxal dimerization and trimerization and 2. Adherence of ring-retaining products with low vapor pressure via gas-particle equilibrium partitioning. However, the molecular weights for glyoxal and methylglyoxal polymers and the uptake rates of glyoxal and methylglyoxal by particle water all were assigned in order to achieve the best possible agreement between simulated and experimental data.

The main goals of this thesis are to: 1.) develop a detailed gas-phase chemistry mechanism for toluene oxidation in the atmosphere through thorough literature review; 2.) predict the SOA formation from toluene by using gas-particle partitioning; 3.) estimate oxidation product contribution to SOA by computationally tracking the structures and the routes of formation; and 4.) investigate quantitatively the impact of NO_x level on SOA yield in toluene oxidation systems. It is hypothesized that bicyclic products from toluene oxidation are significant contributors to SOA formation, based on the research of Suh et al. (2003). It also hypothesized that their formation is controlled by NO_x level, which further leads to control of SOA formation by NO_x.

To model gas-phase chemistry of toluene oxidation, the SOA formation from toluene oxidation, and the impact of NO_x level on SOA yield, an updated version of the Caltech

Atmospheric Chemistry Model (CACM) (Griffin et al., 2002) was applied in this study. CACM tracks the gas-phase chemistry of NO_x, SO_x, and surrogate classes of VOC (toluene treated explicitly in this study) and numerically predicts the concentrations of oxidation products that have the potential to act as constituents of SOA. This model includes more detailed gas-phase chemistry mechanisms than non-specific mechanism models such as SAPRC (Carter, 1990) but provides more simplicity than the completely explicit MCM (Jenkin et al., 2003; Saunders et al., 2003). Through 2008, the explicit gas-phase chemistry of Δ^3-carene (Colville and Griffin, 2004a), α-pinene, β-pinene, d-limonene (Chen and Griffin, 2005), and C_8-C_{17} *n*-alkanes (Jordan et al., 2008) have been incorporated in the original CACM reaction system. An absorptive partitioning model developed by Colville and Griffin (2004b) was used to describe the gas-particle distribution of oxidation products predicted by the updated CACM. In this model, partitioning is driven by product volatility.

Experimental data were provided by the group of Dr. David Cocker at the University of California, Riverside (UCR), and they are used to evaluate the performance of the model. A detailed description of the experimental setup is included here.

2. Methods

2.1 Experimental

Experimental studies of SOA were conducted in the UCR 90-m^3 Indoor Photochemistry Simulator, which was designed specifically for studying ozone and organic aerosol formation at low hydrocarbon and NO_x concentrations under pressure-controlled and temperature-controlled (5-45°C with < ± 1°C) conditions (Carter et al., 2005). This state-of-the-art indoor environmental chamber facility consists of two collapsible 90-m^3 FEP Teflon® film reactors suspended by rigid frames. The top frames can be slowly lowered during experiments to

maintain constant pressure within the reactors and a slightly positive pressure differential between the reactors and the enclosure to minimize dilution and possible contamination from enclosure air. Solar radiation is simulated with either a 200kW Argon arc lamp or multiple black lamps. Before each experiment, the reactors are flushed completely and continuously with purified air generated on site. The unique design of the reactors provides a sufficiently low chamber background, with no detectable VOC (1 ppbC detection limit), NO_x (<1 ppb), or particles (<0.2 particles cm^{-3}) prior to each experiment. All the experiments for this study were conducted in the absence of seed aerosol. Particle wall loss was minimized in chamber experiments by using Teflon® walls and applying large chamber volumes (Carter et al., 2005).

Toluene and hydrogen peroxide (H_2O_2) were the two chemicals injected to the chamber in the experiments and were purchased from Sigma-Aldrich (toluene, > 99.5%; H_2O_2 50 wt% solution in water) (Nakao et al., 2011). The high purity toluene liquid was injected through a heated glass injection manifold system on the first floor of the facility and was flushed into the chamber on the second floor of the facility with pure nitrogen gas (N_2). As described in Nakao et al. (2011), the heated glass manifold was incorporated in a oven (~50-80 °C) and was packed with glass wool to increase the mass transfer area. Loss of toluene in the transfer line and to the wall was considered negligible, based on reasonable agreement between the calculated and observed toluene concentrations. Hydrogen peroxide was used as an OH radical source and was injected through the same oven system. The glass was processed with an acid/base bath and cleaned by water and acetone to enable the H_2O_2 solution to spread. The initial toluene concentration was measured directly in the chambers, and the initial H_2O_2 concentration was calculated based on injection amount. Two hundred and seventy five 115-W Sylvania 350 black lights were used as

the light source for the experiments, and their illumination was considered the start of the experiments. Experiments typically lasted between four and ten hours.

Concentrations of reactants and products were measured using an Agilent 6890 gas chromatograph equipped with a flame ionization detector. Particle size distributions between 27 nm and 686 nm were monitored by a custom-built Scanning Mobility Particle Sizer (SMPS), and particle effective density was measured with an Aerosol Particle Mass Analyzer (APM, Kanomax) and SMPS in series. Measured particle size distributions were based on number concentration as a function of particle radius; particle volume concentrations were calculated assuming particles were spheres. Particle effective densities were as high as approximately 1.8 g cm^{-3} but averaged from 1.3 to 1.4 g cm^{-3}. A constant particle density of 1.4 g cm^{-3} was used to calculate particle mass concentrations.

2.2 Development of gas-phase toluene oxidation mechanism

First, mechanisms of toluene oxidation were incorporated into CACM in detail based on previous experimental and computational studies (Atkinson et al., 1989; Suh et al., 2002; Jenkin et al., 2003; Saunders et al., 2003; Suh et al., 2003). The entire new reaction system includes 82 reactions, 13 assumed non-reacting, fully integrated organic species, 27 reactive, fully integrated secondary organic species, and 25 reactive, organic pseudo-steady state species. The new mechanism is described in detail below.

The oxidation of toluene in the atmosphere is initiated by the reaction with OH (Atkinson et al., 1989). The toluene-OH radical reaction proceeds via two pathways: (1) a minor one (of order 10%) involving H-atom abstraction from C-H bonds of the methyl substituent of the aromatic ring; and (2) a major reaction pathway (of order 90%) involving OH radical addition to the aromatic ring (Atkinson et al., 1989). The H-atom abstraction pathway leads mainly to the

formation of benzaldehyde (C_6H_5CHO). For the OH-addition pathway, there are three possible sites of attack for the OH radical: *o*-, *m*-, and *p*- sites. For toluene, the most energetically favored site for OH attack is the *o*- position (Suh et al., 2002). The resulting OH-adduct can react with either O_2 or (if present) NO_2. The main products of the reactions between the OH adduct and NO_2 are nitroaromatics, such as nitrotoluene. When the OH adduct reacts with O_2, cresols or peroxy radicals are formed. The peroxy radicals are believed to cyclize, forming bicyclic radicals. The bicyclic radicals can be further oxidized by O_2 to form bicyclic peroxy radicals, which are expected to react with NO, NO_3 or other peroxy radicals to form stable products or bicyclic oxy radicals. The formed bicyclic oxy radicals will undergo favored β-scission reactions to generate ring fragmentation products, mainly glyoxal, methylglyoxal, methyl butenedial, and 1, 4-butenedial. The β-scission products were lumped, and when they were allowed to react with OH, it was assumed that a certain percentage of their mass formed non-volatile SOA. This percentage was used as a fitting parameter for the model and is described subsequently, as it does not affect simulated NO_2, O_3, or toluene mixing ratios significantly. Illustrative reaction pathways for toluene oxidation are given in Figures 1, 2, and 3.

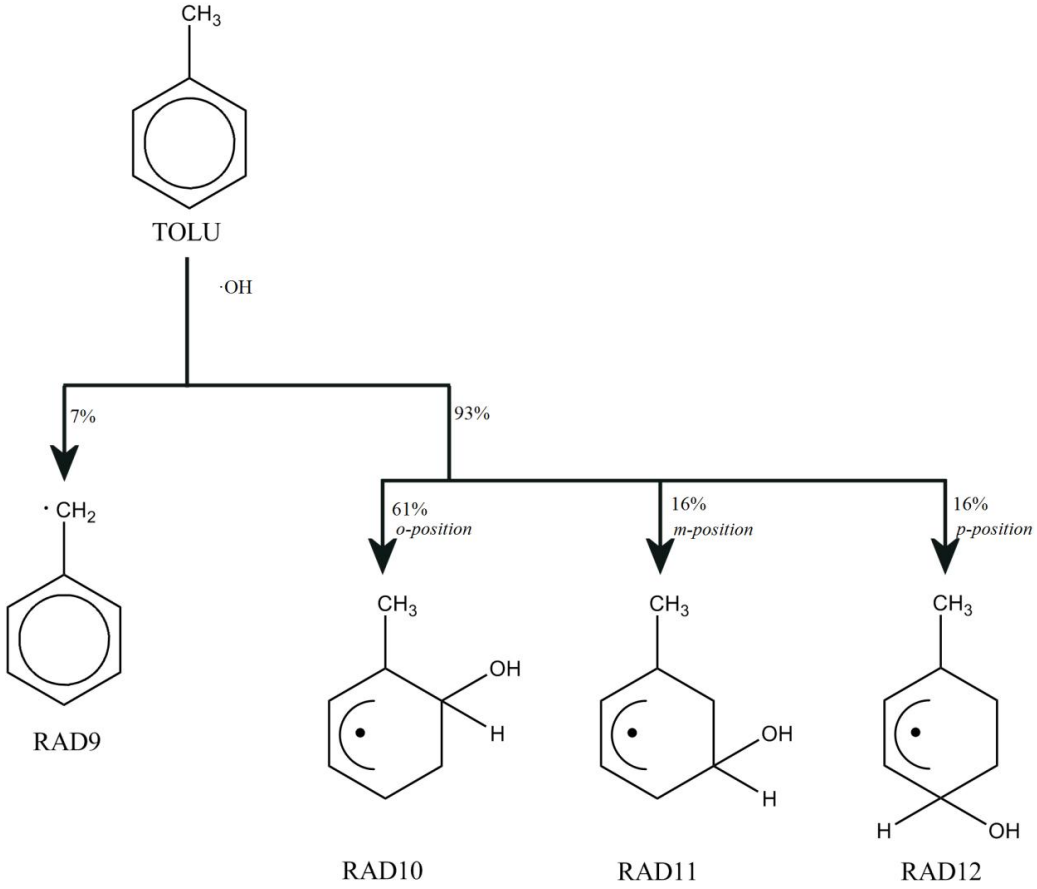

Fig. 1. OH-initiated toluene oxidation. The branching ratio for each pathway is shown in percentage.

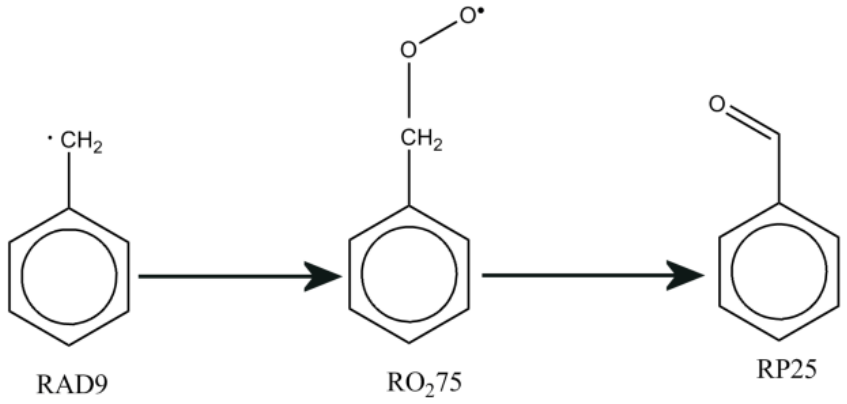

Fig. 2. H-abstraction pathway.

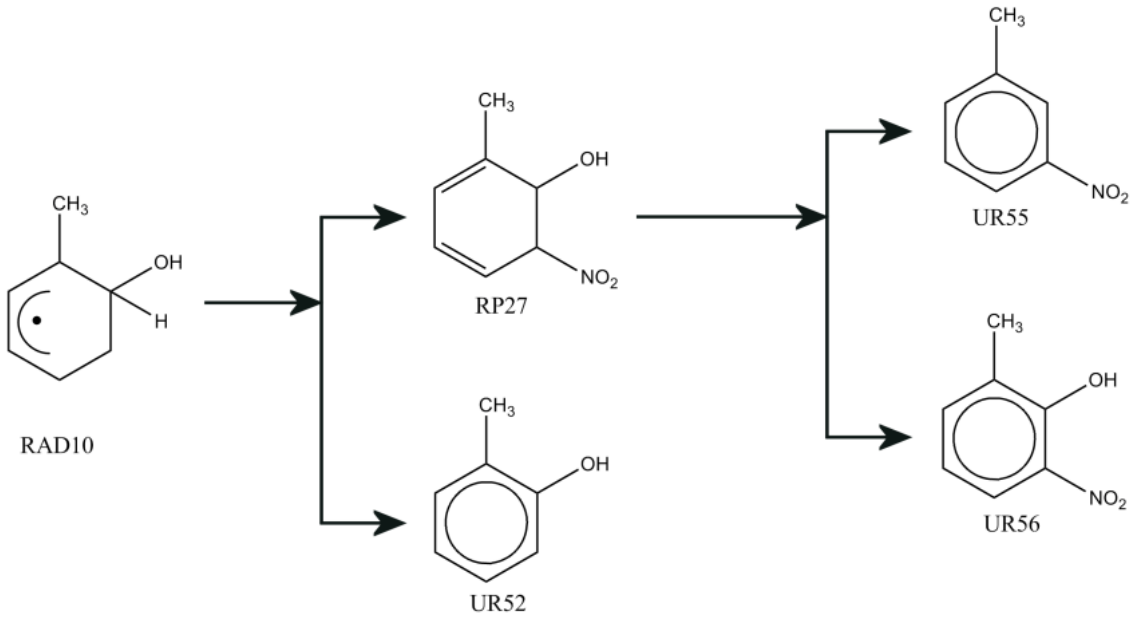

Fig. 3a. OH-addition pathway: OH-*o*-adducts with NO_2.

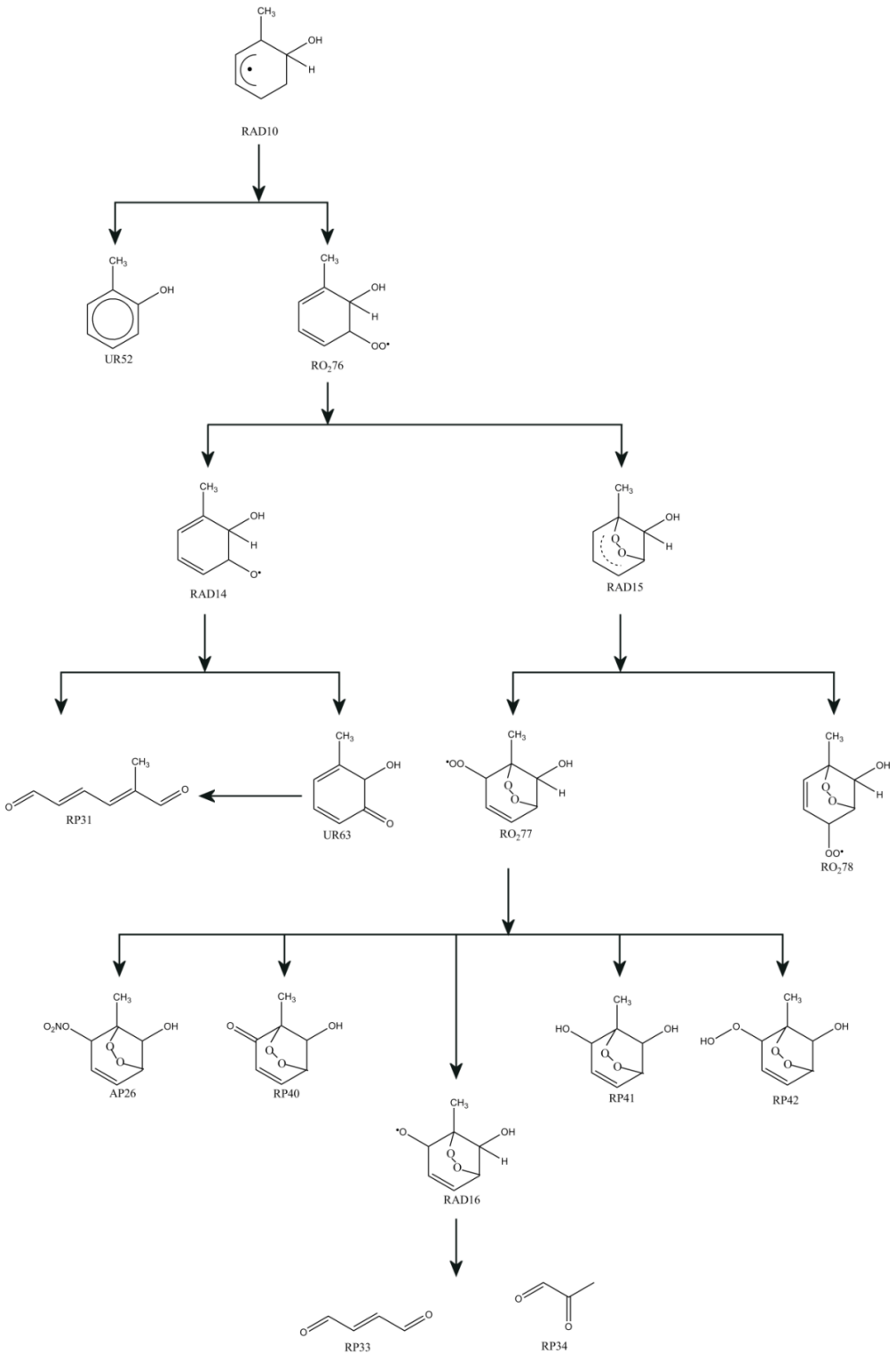

Fig. 3b. OH-addition pathway: OH-*o*-adducts with O_2.The explicit reaction pathways are only shown for $RO_2$77, and $RO_2$78 is assumed to have similar reaction mechanisms as $RO_2$77.

For each reaction, any applicable branching ratios and rate constants are given specifically in Table 1a and b. The reactants, products, branching ratios, and reaction rate constants have been incorporated appropriately into the computational code for CACM, in which kinetic rate expressions for concentrations of all gas-phase species as a function of time are solved. For organic radical species, concentrations are not determined in this manner but rather through assumption of steady-state.

Table 1a

Toluene oxidation reactions.

Reaction Index	Reactants	Products	Rate Constants, [a] cm^3 $molecule^{-1}$ s^{-1}
401	TOLU + OH	CF(80)*RAD9+CF(80)*H_2O++CF(81)*RAD10+ CF(82)*RAD11+CF(83)*RAD12	1.8E-12*EXP(338/TEMP)
402	RAD9 + O_2	$RO_2$75 + RO_2T	1.00E+06
403	$RO_2$75 + RO_2T	CF(84)*RP24+CF(85)*RP25+CF(86)*RAD13	1.30E-12
404	RP24 + OH	RP25 + HO_2	8.93E-12
405	RAD13 + O_2	RP25 + HO_2	6.0E-14*EXP(-550/TEMP)
406	$RO_2$75 + NO	CF(87)*AP25 + CF(88)*RAD13+CF(88)*NO_2	2.54E-12*EXP(360/TEMP)
407	AP25	RAD13 + NO_2	1
408	AP25 + OH	RP25 + NO_2 + H_2O	6.03E-12
409	$RO_2$75 + NO_3	RAD13 + NO_2	2.50E-12
410	$RO_2$75 + HO_2	RP26 + O_2	2.91E-13*EXP(1300/TEMP)*0.82
411	RP26	RAD13 + OH	1
412	RP26 + OH	PR25 + H_2O + OH	2.05E-11
413	RAD10 + NO_2	CF(89)*RP27 + CF(90)*UR52 + CF(90)*HONO	3.60E-11
414	RAD11 + NO_2	CF(91)*RP28 + CF(92)*RP29+ CF(93)*UR53 + CF(93)*HONO	3.60E-11
415	RAD12 + NO_2	CF(94)*RP30 + CF(95)*UR54 + CF(95)*HONO	3.60E-11
416	RP27	CF(96)*UR55 + CF(96)*H_2O + CF(97)*UR56 + CF(97)*H_2	1.00E+06
417	RP28	CF(98)*UR57 + CF(98)*H_2O + CF(99)*UR58 + CF(99)*H_2	1.00E+06
418	RP29	CF(100)*UR59 + CF(100)*H_2O + CF(101)*UR60 + CF(101)*H_2	1.00E+06
419	RP30	CF(102)*UR61 + CF(102)*H_2O + CF(103)*UR62 + CF(103)*H_2	1.00E+06

420	RAD10 + O_2	CF(104)*UR52 + CF(104)*H_2O + CF(105)*$RO_2$76 + CF(105)*RO_2T	5.20E-16
421	$RO_2$76 + NO	RAD14 + NO_2	1.10E-11
422	RAD14 + O_2	UR63 + HO_2	1.00E+06
423	RAD14	RP31 + HO_2	1.00E+06
424	$RO_2$76 + RO_2T	RAD15	260
425	RAD15 + O_2	CF(106)*$RO_2$77 + CF(106)*RO_2T + CF(107)*$RO_2$78 + CF(107)*RO_2T	1.00E-17
426	$RO_2$77 + RO_2T + NO	CF(119)* AP26 + CF(120)* RAD16 + CF(120) * NO_2	2.54E-12*EXP(360/TEMP)
427	$RO_2$78 + RO_2T + NO	CF(124)* AP27 + CF(125)* RAD17 + CF(125) * NO_2	2.54E-12*EXP(360/TEMP)
428	RAD11 + O_2	CF(108)*UR53 + CF(108)*HO_2 + CF(109)*$RO_2$79 + CF(109)*RO_2T	5.20E-16
429	$RO_2$79 + RO_2T + NO	RAD18 + NO_2	1.10E-11
430	RAD18 + O_2	UR64 + HO_2	1.00E+06
431	RAD18	RP31 + HO_2	1.00E+06
432	$RO_2$79 + RO_2T	RAD19	260
433	RAD19 + O_2	CF(110)*$RO_2$80 + CF(110)*RO_2T + CF(111)*$RO_2$81 + CF(111)*RO_2T	1.00E-17
434	$RO_2$80 + RO_2T + NO	CF(129)* AP28 + CF(130)* RAD20 + CF(130)*NO_2	2.54E-12*EXP(360/TEMP)
435	$RO_2$81 + RO_2T + NO	CF(134)* AP29 + CF(135)* RAD21 + CF(135)*NO_2	2.54E-12*EXP(360/TEMP)
436	RAD12 + O_2	CF(112)*UR54 + CF(112)*HO_2 + CF(113)*$RO_2$82 + CF(113)*RO_2T	5.20E-16
437	$RO_2$82 + NO + RO_2T	RAD22 + NO_2	1.10E-11
438	RAD22 + O_2	UR56 + HO_2	1.00E+06
439	RAD22	RP32 + HO2	1.00E+06
440	$RO_2$82 + RO2T	RAD23	2.60E+02
441	RAD23 + O_2	$RO_2$83 + RO_2T	1.00E-17
442	$RO_2$83 + RO_2T + NO	CF(138)* AP30 + CF(139)* RAD24 + CF(139)*NO_2	2.54E-12*EXP(360/TEMP)
443	$RO_2$76 + RO_2T	RAD14 + O_2	1.00E-15
444	$RO_2$79 + RO_2T	RAD18 + O_2	1.00E-15
445	$RO_2$82 + RO_2T	RAD22 + O_2	1.00E-15
446	$RO_2$77 + RO_2T	CF(121)*RAD16 + CF(122)*RP41 + CF(123)*RP40	8.80E-13
447	$RO_2$80 + RO_2T	CF(131)*RAD20 + CF(132)*RP47 + CF(133)*RP46	8.80E-13
448	$RO_2$83 + RO_2T	CF(140)*RAD24 + CF(141)*RP52 + CF(142)*RP51	8.80E-13
449	RAD16	RP33 + RP34 + HO_2	1.00E+06
450	RAD17	CF(114)*RP35 + CF(114)*RP36 + CF(115)*RP35 + CF(115)*RP37 + CF(116)*RP34 + CF(116)*RP33 + CF(117)*RP35 + CF(117)*RP38 + CF(118)*RP34 + CF(118)*RP39 + HO_2	1.00E+06

451	RAD20	RP38 + RP35 + HO_2	1.00E+06
452	RAD21	RP37 + RP35 + HO_2	1.00E+06
453	RAD24	RP38 + RP35 + HO_2	1.00E+06
454	WALL + HV	HONO	1.50E-05
455	$RO_2$77 + RO_2T + HO_2	RP42	2.91E-13*EXP(1300/TEMP)
456	$RO_2$77 + RO_2T + NO_3	RAD16 + NO_2	2.50E-12
457	AP26 + OH	RP40 + NO_2	7.16E-11
458	RP42 + OH	RP40 + OH	9.64E-11
459	AP27 + OH	RP43 + NO_2	7.16E-11
460	$RO_2$78 + RO_2T	CF(126)*RAD17 + CF(127)*RP44 + CF(128)*RP43	8.80E-13
461	$RO_2$78 + RO_2T + HO_2	RP45	2.91E-13*EXP(1300/TEMP)
462	RP45 + OH	RP43 + OH	9.64E-11
463	$RO_2$78 + RO_2T + NO_3	RAD17 + NO_2	2.50E-12
464	AP28 + OH	RP46 + NO_2	7.16E-11
465	$RO_2$80 + RO_2T + HO_2	RP48	2.91E-13*EXP(1300/TEMP)
466	RP48 + OH	RP46 + OH	9.64E-11
467	$RO_2$80 + RO_2T + NO_3	RAD20 + NO_2	2.50E-12
468	$RO_2$81 + RO_2T	CF(136)*RAD21 + CF(137)*RP49	8.80E-13
469	$RO_2$81 + RO_2T + HO_2	RP50	2.91E-13*EXP(1300/TEMP)
470	$RO_2$81 + RO_2T + NO_3	RAD21 + NO_2	2.50E-12
471	AP30 + OH	RP51 + NO_2	7.16E-11
472	$RO_2$83 + RO_2T + HO_2	RP53	2.91E-13*EXP(1300/TEMP)
473	RP53 + OH	RP51 + OH	9.64E-11
474	$RO_2$83 + RO_2T + NO_3	RAD24 + NO_2	2.50E-12
475	DICARBONYL PRODUCTS + OH	RP54	(5.2E-11*0.83*0.21 + 1.91E-12*EXP(575/TEMP)*0.25 + 3.1E-12*EXP(340/TEMP)*0.6*0.29 + 6.2E-11*0.52*0.08 + 4.4E-11*0.385*0.17)*0.1
476	UR63 + NO	RP31 + NO	1.00E+06
477	UR64 + NO	RP31 + NO	1.00E+06
478	UR65 + NO	RP32 + NO	1.00E+06
479	RP27 + O_2 + NO	RP31 + HONO + NO_2	1.00E+06
480	RP28 + O_2 + NO	RP32 + HONO + NO_2	1.00E+06
481	RP29 + O_2 + NO	RP31 + HONO + NO_2	1.00E+06
482	RP30 + O_2 + NO	RP32 + HONO + NO_2	1.00E+06

[a] The model requires rate constants in ppm min^{-1} units. To convert from cm^3 $molecule^{-1}$ s^{-1} to ppm min^{-1}, multiply by 4.4E+17/TEMP. CF(*i*) represents product stoichiometric yields.

Table 1b.

Product stoichiometric yields of toluene oxidation reactions.

Branching Ratio	Value
CF(80)	0.07
CF(81)	0.61
CF(82)	0.16
CF(83)	0.16
CF(84)	0.2
CF(85)	0.2
CF(86)	0.6
CF(87)	0.105
CF(88)	0.895
CF(89)	0.2
CF(90)	0.8
CF(91)	0.157
CF(92)	0.043
CF(93)	0.8
CF(94)	0.2
CF(95)	0.8
CF(96)	0.5
CF(97)	0.5
CF(98)	0.5
CF(99)	0.5
CF(100)	0.5
CF(101)	0.5
CF(102)	0.5
CF(103)	0.5
CF(104)	0.22
CF(105)	0.78
CF(106)	0.5
CF(107)	0.5
CF(108)	0.22
CF(109)	0.78
CF(110)	0.5
CF(111)	0.5
CF(112)	0.22
CF(113)	0.78
CF(114)	0.2
CF(115)	0.2
CF(116)	0.2
CF(117)	0.2
CF(118)	0.2

CF(119)	0.111
CF(120)	0.889
CF(121)	0.6
CF(122)	0.2
CF(123)	0.2
CF(124)	0.111
CF(125)	0.889
CF(126)	0.6
CF(127)	0.2
CF(128)	0.2
CF(129)	0.111
CF(130)	0.889
CF(131)	0.6
CF(132)	0.2
CF(133)	0.2
CF(134)	0.111
CF(135)	0.889
CF(136)	0.75
CF(137)	0.25
CF(138)	0.111
CF(139)	0.889
CF(140)	0.6
CF(141)	0.2
CF(142)	0.2

The experimental data for this study were obtained through experiments conducted at UCR. Among seven experiments conducted by UCR with toluene and H_2O_2 as initial reactants, Experiment 1141B (Table 2) was used as the base case for model development.

Table 2

Initial conditions of all toluene + H_2O_2 experiments.

Experiment ID	Date	Initial Concentration (ppb)		
		Toluene	H_2O_2	O_3
1141B	March 13, 2010	85.0	3044.2	10.8
1149B	March 21, 2010	82.7	5073.6	16.1
1251B	August 19, 2010	84.0	1014.7	0.0
1266A	September 5, 2010	119.8	1014.7	3.3
1290B	October 6, 2010	432.2	1014.7	6.1
1477A	July 26, 2011	114.7	1014.7	1.6

1477B	July 26, 2011	274.4	1014.7	0.0

For all seven experiments, the initial NO_x levels were below the detection limit of the analytical equipment, which was less than 1 ppb. Even with nearly zero NO_x initial concentrations, all experimental data showed that there was significant NO_x participating in the experiments (above detection limits). Thus, a wall reaction was considered as a source of HONO (Whitten et al., 2010):

$$\text{Wall} + h\nu \rightarrow \text{HONO}$$

However, the rate constant of this wall reaction was not determined. Different rate constant values were tested in the model, and the optimized rate constant was determined to be 1.5×10^{-5} ppb s^{-1} when the simulated ozone and NO_2 showed good fit to experimental gas-phase data for Experiment 1141B. (Differences between simulated and experimental O_3 and NO_2 were within 15% of the experimental values.)

2.3 Development of gas-particle partitioning model

Once gas-phase modeled concentrations of NO, NO_2, O_3, and toluene compared favorably to experimental data for the designated base case (described subsequently), the results from CACM for semi-volatile SOA species were linked to a partitioning model to estimate SOA formation. Secondary organic oxidation products can partition between the gas phase and condensed organic material (om) at concentrations below saturation. To calculate the partitioning and formation of SOA, a model developed by Colville and Griffin (2004b) and suitable for chamber studies was applied. Two assumptions are made: 1.) the condensed aerosol phase is liquid due to freezing point depression in a complex mixture (Covington and Dickinson, 1973) and 2.) absorption to a liquid phase is the dominant mechanism of partitioning (Pankow, 1994a,b). For a

compound i, the equilibrium partitioning coefficient is defined as (Pankow, 1994a,b; Odum et al., 1996)

$$K_{om,i} = \frac{RT}{MW_{om}\, 10^6 \gamma_i P_{L,i}^{\circ}}, (1)$$

where $K_{om,i}$ (m^3 μg^{-1}) is the temperature-dependent partitioning coefficient for compound i, R is the ideal gas constant (8.206×10^{-5} m^3 atm mol^{-1} K^{-1}), T is the temperature (K), MW_{om} is the average molecular weight of the om phase (g mol^{-1}), 10^6 is a constant to convert grams to micrograms, γ_i is the activity coefficient of compound i in the om phase, and $P_{L,i}^{\circ}$ is the sub-cooled liquid vapor pressure (atm) of compound i at temperature T. Meanwhile, the gas-particle partitioning coefficient can also be defined as

$$K_{om,i} = \frac{A_i}{G_i M_\circ}, (2)$$

where A_i ($\mu g\ m^{-3}$) and G_i ($\mu g\ m^{-3}$) are the concentrations of compound i in the aerosol phase and gas phase, respectively, and $M_\circ$ ($\mu g\ m^{-3}$) is the total concentration of organic aerosol mass present, including both primary organic aerosols (POA) and SOA (Pankow, 1994a,b). The following expression will also hold, based on mass conservation principles:

$$C_i = A_i + G_i, (3)$$

where C_i ($\mu g\ m^{-3}$) is the total concentration of compound i. In these chamber studies, the lack of POA indicates that

$$M_\circ = \sum_{i=1}^{N} A_i\,, (4)$$

where N is the total number of compounds partitioning to the aerosol phase.

Combining Eqs. (1) through (4) results in the following equation, which is solved iteratively for SOA mass using an adapted bisection method:

$$\sum_{i=1}^{N} \frac{K_{om,i} C_i}{1 + K_{om,i} M_\circ} - 1 = 0, (5)$$

The calculation of partitioning coefficients requires the vapor pressures of the compounds of interest. However, the bicyclic products have unusual molecular structures and experimentally determined vapor pressures are not available from the existing literature. Therefore, the method of Mydal and Yalkowsky (1997) was applied in this study, which calculates vapor pressure from the effective number of torsional bonds, hydrogen bond number, and boiling point temperature. However, for the compounds for which vapor pressures are not available, the boiling point temperatures generally are not available as well. To calculate the boiling point temperatures, an empirical method depending on molecular size and structure developed by Cordes and Rarey (2002) was used. To evaluate the accuracy of the Myrdal and Yalkowsky (1997) method, it was applied to calculate the vapor pressures of the species in this study with vapor pressures available from experimental data. The average ratio of the calculated vapor pressure to the experimental vapor pressure was 35. Thus, calculated vapor pressures for those species lacking experimental data were divided by 35 universally. This correction (which also accounts for deviation of activity coefficients from unity) is significantly smaller than similar correction factors that have been used in the past (e.g., Jordan et al., 2008).

2.4 Non-volatile SOA

After CACM was adapted for the wall reaction as described previously and the calculated vapor pressures were decreased by a factor of 35, the SOA simulation for the base case of Experiment 1141B indicated a best fit appeared when 10% of the OH reaction with β-scission products (typically dicarbonyls) lead to non-volatile SOA. This is believed to account for heterogeneous and/or oligomerization reactions discussed by Cao and Jang (2010). The fitting

parameter of 10% is also a reasonable estimation based on laboratory observations. It was observed that acetylene (C_2H_2) formed glyoxal (CHOCHO) through OH-initiated oxidation and that more than 99% of SOA formed from C_2H_2 was attributed to CHOCHO (Volkamer et al., 2009). Furthermore, SOA yields from CHOCHO ranged from 1% to 24% (Volkamer et al., 2009); the fitted parameter of 10% falls within this observed range.

3. Results

3.1 Comparison of measured and simulation data for base case

The comparison results for the base case are shown in Figures 4, 5, 6 and 7. From the simulation results, it is shown that for toluene concentration, the variance between the model and the simulation was within 5%. Predicted SOA, O_3 and NO_2 concentrations are typically within 15% of the experimental values at the end of simulation.

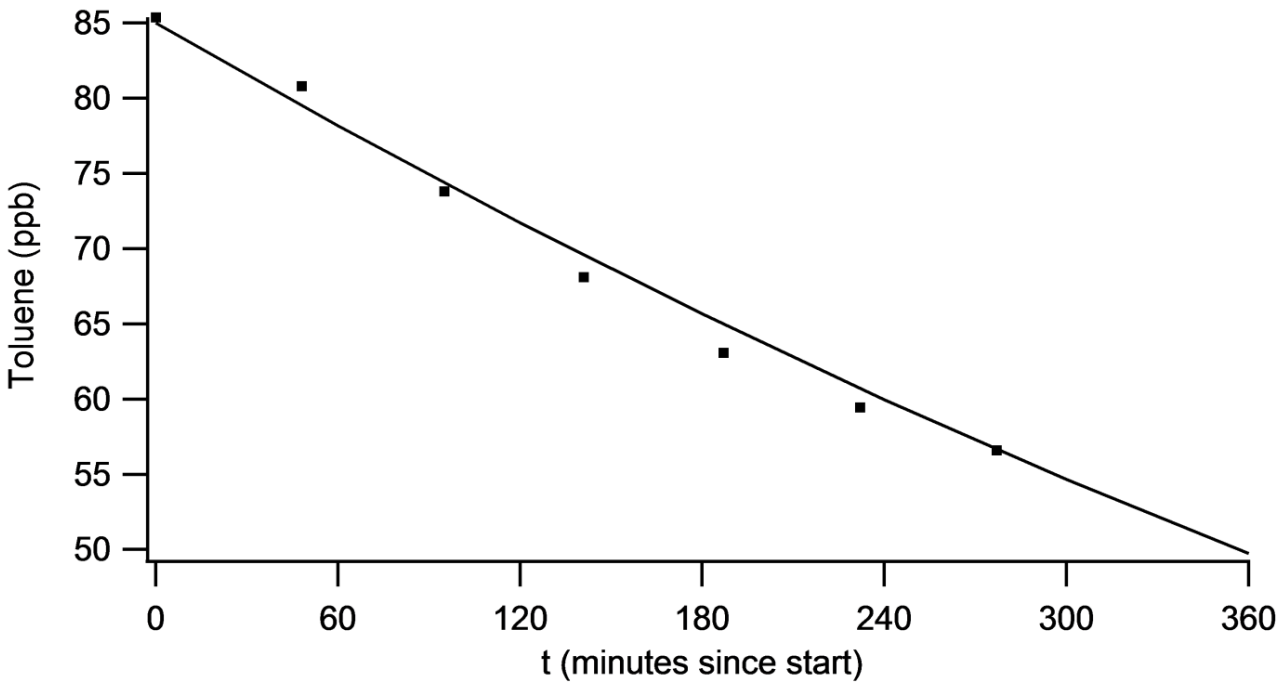

Fig. 4. Comparison of measured (squares) and modeled (line) toluene concentrations during Experiment 1141B.

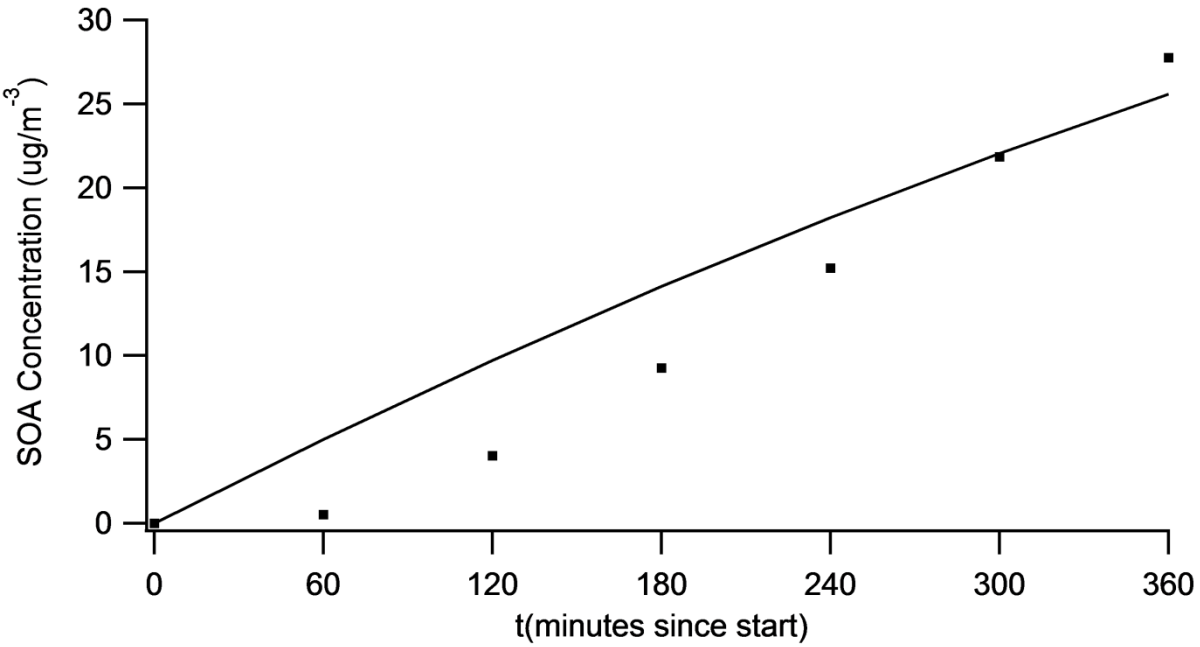

Fig. 5. Comparison of measured (squares) and modeled (line) SOA concentrations during Experiment 1141B.

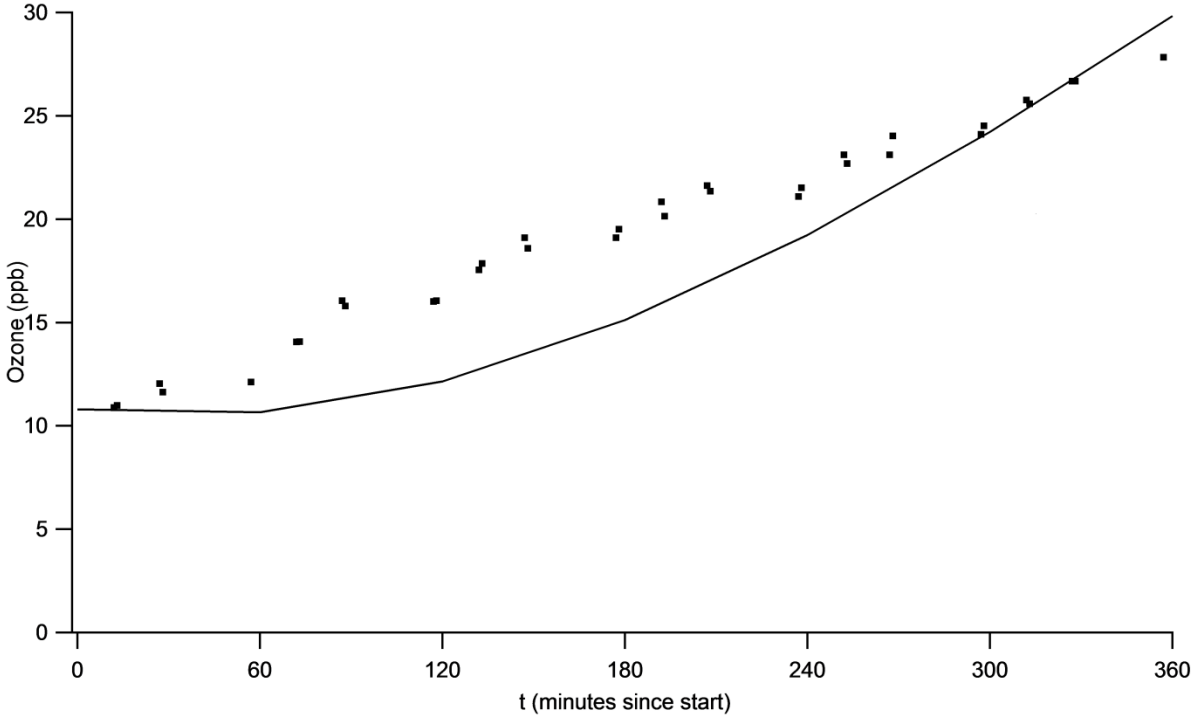

Fig. 6. Comparison of measured (squares) and modeled (line) ozone concentrations during Experiment 1141B.

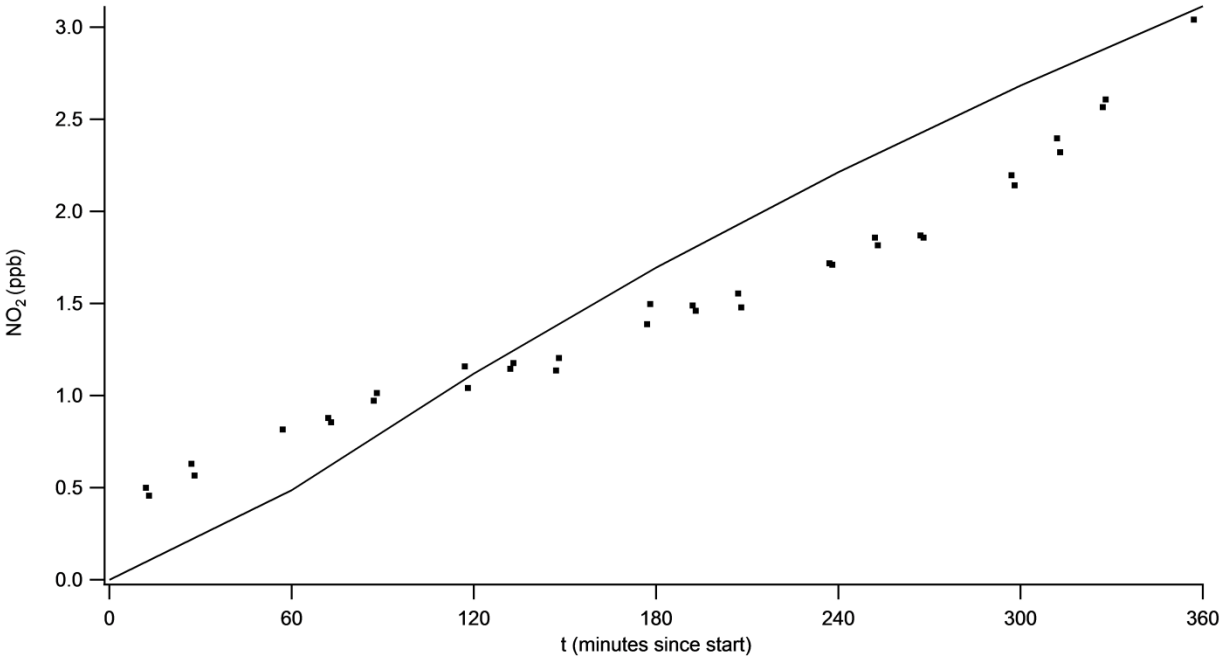

Fig. 7. Comparison of measured (dots) and modeled (line) NO_2 concentrations during Experiment 1141B.

3.2 Comparison of experiments and simulations of toluene and SOA for all experiments

To evaluate the more general performance of the toluene oxidation model, experimental data and simulation results were compared for toluene consumption and SOA formation for all seven experiments. The initial reactants for all experiments were toluene and H_2O_2, and some of the experiments had initial ozone concentrations. Photolysis of H_2O_2 provided the OH. For each experiment, the initial toluene concentration was the measured concentration in the chamber, and the initial H_2O_2 concentration was calculated based on injection volume and chamber volume. Ozone and NO_2 concentrations also were measured for all experiments. For any initial ozone and NO_2 less than 1 ppb, initial concentrations were considered to be zero. Initial conditions for all the experiments are listed in Table 2.

The durations of experiments ranged from 4 to 10 hours, and the measurement resolution varied from 1 minute for O_3, NO_2, and SOA to 30 minutes for toluene. Toluene simulations were based on mechanisms described in Section 2.1, and SOA simulations were based on the gas-phase partitioning model described in Section 2.2. The duration of each simulation was six model hours, and the results were output every hour of model time.

The comparison between experimental and simulation data shows that the model was able to simulate toluene consumption, with the differences generally within ±5% of the experimental data throughout the entire simulation periods. The percentage difference was calculated by

$$\text{Percentage Difference} = \frac{Simulation\ Data - Experimental\ Data}{Experimental\ Data} \times 100\%, \quad (6)$$

For all the seven experiments, the toluene simulation results are listed in Table 3.

Table 3

Toluene simulation results.

Experiment ID	Min of Percent Difference	Max of Percent Difference	Average of Percent Difference	Min of Absolute Percent Difference	Max of Absolute Percent Difference	Average of Absolute Percent Difference
1141B	-1.86%	3.68%	0.89%	0.35%	3.68%	1.95%
1149B	-5.68%	0.60%	-1.09%	0.04%	5.68%	1.34%
1251B	-7.17%	0.00%	-3.42%	0.00%	7.17%	3.42%
1266A	-0.61%	2.72%	1.21%	0.00%	2.72%	1.38%
1290B	-5.07%	2.53%	-0.12%	0.00%	5.07%	1.92%
1477A	-1.93%	2.20%	0.80%	0.00%	2.20%	1.29%
1477B	-2.28%	0.64%	-0.25%	0.00%	2.28%	0.56%
Average	-3.52%	1.77%	-0.28%	0.06%	4.12%	1.69%
Min	-7.17%	0.00%	-3.42%	0.00%	2.20%	0.56%
Max	-0.61%	3.68%	1.21%	0.35%	7.17%	3.42%

The distribution of percentage difference of toluene simulation for all available experiment-simulation pairs are given in Figure 8.

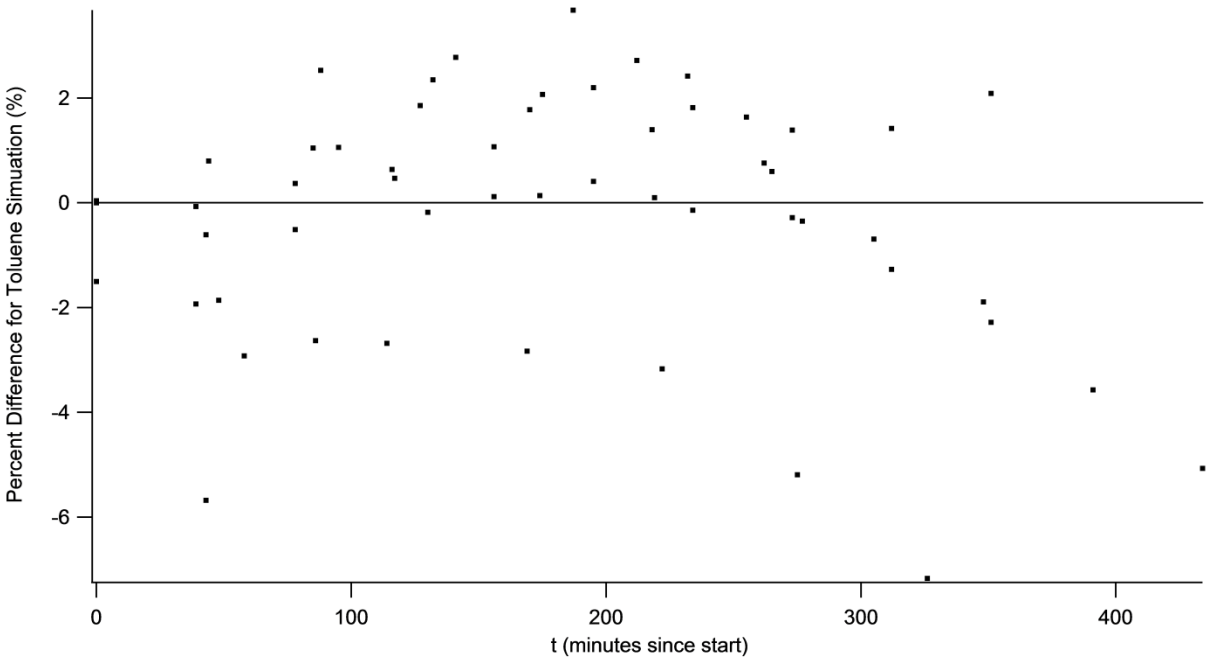

Fig. 8. Distribution of percent difference for toluene simulations.

For the seven experiments, there were total 59 pairs of experiment-simulation data. There is no obvious distribution pattern for the percent difference. The majority of the percentages lie between ±3% (52 out of 59), with a few with an absolute value larger than 5% (4 out of 59). The average of the percent difference is -0.10%, and the average of the absolute percent different is 1.6%, which indicates that the toluene simulation is very close to the experimental toluene concentrations. This represents a significant improvement over Cao and Jang (2010). The detailed statistics are listed in Table 4.

Table 4

Statistics of distribution of percent difference of toluene simulation.

Percentage Interval	Count of Percent Difference
$(-\infty,-5\%] \cup [5\%, \infty)$	4
[-1%,1%]	24
[-2%,-1%] ∪ [1%, 2%]	15
[-3%,-2%] ∪ [2%, 3%]	13
[-4%,-3%] ∪ [3%, 4%]	3

Total count	59
Minimum	-7.17%
Maximum	3.68%
Average of Absolute Percent Difference	1.63%
Average	-0.10%

A direct comparison between this study and other studies is difficult because the studies were conducted under different conditions (temperature, humidity, NO_x level, light intensity, and inclusion of aerosol seeds). However, to provide further validation for the gas-phase chemistry mechanism developed for toluene oxidation, the gas-partitioning model was turned off for the base case. The gas-phase product yields were calculated and compared with previous studies (Atkinson, 1990). Atkinson (1990) summarized observed ring-retaining product yields from OH radical initiated reactions of aromatic hydrocarbons under atmospheric conditions. The comparison results are shown in Table 5. Our gas-phase chemistry model successfully predicted all major ring-retaining products from toluene oxidation, except the yields of nitrogen-containing aromatics were comparatively small in the model. However, this makes sense given the very low NO_x level in the base case. For further validation, the simulated ring-opening products from toluene oxidation were also compared with recent experimental observation (Alvarez et al., 2007). In Alvarez et al. (2007), the experimental yields for butenedial, glyoxal, methylglyoxal and 4-oxo-2-pentenal were 13%, 37%, 37% and 13.8% respectively. The simulated yields for the four dicarbonyls were 0.44%, 0.60%, 0.51%, and 0.17%, respectively. The absolute yield differences between experimental observations and simulation results can be explained simply by particle formation. However, the ratios of yields to each other for these four dicarbonyls showed good agreement between experiment and simulation (e.g., methylglyoxal : 4-oxo-2-pentenal = 3:1 for both experiment and simulation).

Table 5

Comparison between literature yields and model yields of gas-phase reaction products.

Product	Yield range from literatures	Model yield
Benzaldehyde	0.054 ~ 0.12	0.04269
Benzyl nitrate	0.007 ~ 0.0084	0.00013
o-cresol	0.131 ~ 0.22	0.13438
m- + *p*- cresol	0.048 ~ 0.05	0.07050
m-nitrotoluene	0.0135	5.67101E-06

The same analyses were conducted for SOA simulation results. There are 37 pairs of experiment-simulation data available for SOA. The SOA simulation results are listed in Table 6.

Table 6

SOA simulation results.

Experiment ID	Min of Percent Difference	Max of Percent Difference	Average of Percent Difference	Min of Absolute Percent Difference	Max of Absolute Percent Difference	Average of Absolute Percent Difference
1141B	-7.82%	851.35%	176.29%	0.84%	851.35%	178.90%
1149B	-0.14%	52831.37%	13241.85%	0.14%	52831.37%	13241.91%
1251B	7.11%	715.56%	202.28%	7.11%	715.56%	202.28%
1266A	22.60%	479.99%	150.21%	22.60%	479.99%	150.21%
1290B	-29.56%	167.31%	10.88%	3.65%	167.31%	46.10%
1477A	-14.44%	2816.94%	482.10%	4.64%	2816.94%	492.74%
1477B	-23.70%	306.63%	48.53%	1.48%	306.63%	68.65%
Average	-6.56%	8309.88%	2044.59%	5.78%	8309.88%	2054.40%
Min	-29.56%	167.31%	10.88%	0.14%	167.31%	46.10%
Max	22.60%	52831.37%	13241.85%	22.60%	52831.37%	13241.91%

Compared to toluene simulations, SOA simulations exhibit much larger absolute percent differences, with the maximum absolute percent difference of 13241.91% and average absolute percent difference of 2054.40%, which indicate that the model over predicts SOA formation by as much as a factor of 132 and on average by a factor of more than 20. However, these error numbers are dominated by the large difference at the early stages of the simulations, especially for the first two hours of the simulation, as shown in Figure 9 and Table 7.

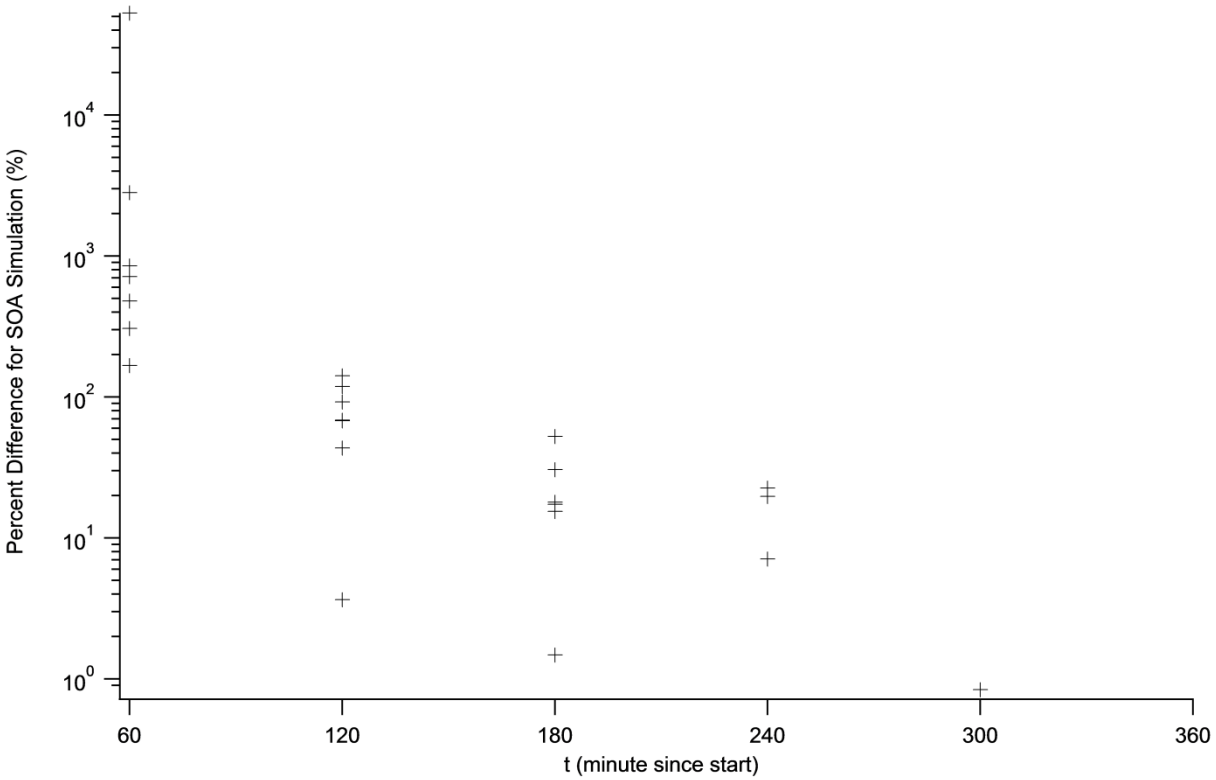

Fig. 9. Distribution of percent difference for SOA simulations.

Table 7

Counts of SOA absolute percent difference for intervals.

Minutes	Interval > 100%	[50%, 100%]	[20%, 50%]	[10%, 20%]	<10%	Grand Total
60	7					7
120	2	3	1		1	7
180		1	2	3	1	7
240			2	2	3	7
300			2	1	1	4
360			2	1	1	4
Grand Total	**9**	**4**	**9**	**7**	**7**	**36**

Figure 9 indicates that the absolute percent difference decreases significantly as a function of time as the particles grow and condensation becomes a more important growth mechanism. All

absolute percent differences larger than 100% occur within the first 2 hours. Detailed breakdowns of absolute percent difference for defined intervals are shown in Table 7. Again, nine of 36 absolute percent differences are larger than 100%, and they all occur within the first two hours of simulation. As simulations proceed, more absolute percent differences fall into the interval of 10 to 20%. The time-specific averages of all absolute percent differences are listed in Table 8; the average percent difference tends to be approximately 15% when simulations pass four hours.

Table 8

Absolute percent difference at the end of SOA simulation for each experiment.

Experiment ID	Length of Simulation (min)	Absolute Percent Difference at End of Simulation
1141B	360	7.82%
1149B	240	0.14%
1251B	240	7.11%
1266A	240	22.60%
1290B	360	24.94%
1477A	360	14.44%
1477B	360	23.70%
Average	309	14.39%

The over prediction of SOA at the early stage of the experiments potentially is caused by the following: 1.) inappropriate experimental particle wall loss correction for very small particles (All data are wall-loss corrected.); 2.) heteromolecular nucleation was not simulated explicitly in the model, which by necessity was an important SOA growth mechanism in the early stages; and 3.) the Kelvin effect was not incorporated in the model. The small particle radius at the early stage of SOA formation forces species to favor the gas phase, which causes slow growth of SOA at the early stage of experiments.

Based on the above discussion, the absolute percent difference at the end of each simulation is used to evaluate the model performance. These results are listed in Table 8. Generally the model gives very good prediction for SOA formation, with an average difference less than ± 15%. The chemical species contributing more than 1% of the SOA at end of each hour are listed in Table 9.

Table 9.

Chemical species' contributions to SOA.

	Fraction of SOA					
Chemical Species	t = 60 min	t = 120 min	t = 180 min	t = 240 min	t = 300 min	t = 3600 min
RP42	32.4%	32.4%	32.4%	32.3%	32.3%	32.3%
RP45	32.4%	32.4%	32.4%	32.3%	32.3%	32.3%
RP48	8.5%	8.5%	8.5%	8.5%	8.5%	8.5%
RP50	8.6%	8.6%	8.6%	8.6%	8.6%	8.6%
RP53	17.0%	17.0%	17.0%	17.0%	17.0%	16.9%
Total	98.9%	98.9%	98.8%	98.7%	98.7%	98.6%

It is shown that all listed species were bicyclic products of bicyclic peroxy radicals reacting with HO_2 (Reaction 455, 461, 465, 469, 472), and the fractions remain almost constant as simulations proceed. Bicyclic products are predicted to dominate SOA formation, contributing more than 98% of SOA formed. From this finding, it is expected that any changes that alter the bicyclic peroxy radicals plus HO_2 reaction would have a significant impact on SOA formation. Even though it was observed that 3-methyl-2,5-furandione and dihydro-2,5-furandione composed 46% of the identified SOA composition (Forstner et al., 1997), Jang and Kamens (2001) pointed out that less than 0.02% of these two compounds would be expected in the aerosol phase based on vapor pressures (Jang and Kamens, 2001), which contradicts the observations of Forstner et al. (1997). Therefore, the exact speciation of toluene-derived SOA remains uncertain. Furthermore,

Jang and Kamens (2001) confirmed the importance of bicyclic products (e.g., methylcyclohexenetriones) in SOA formation, validating the importance of bicyclic products.

3.3 SOA Yield at different NO_x levels

It has been shown that aromatic oxidation and subsequent SOA formation is impacted by varying NO_x level (Ng et al., 2007). Therefore, our model is applied to investigate the impact of NO_x level on toluene oxidation and subsequent SOA formation. The original data of Experiment 1141B were used as a benchmark for this study, and the NO_x level was increased to the levels indicated in Table 10 while keeping other conditions unchanged.

Table 10

NO_x levels for NO_x case study.

Case ID	Initial NO_x Level
1 (Base Case)	NO_x = 0 ppb
2	NO = 50 ppb
3	NO_2 = 50 ppb
4	NO = 25 ppb, NO_2 = 25 ppb
5	NO = 100 ppb
6	NO_2 = 100 ppb
7	NO = 50 ppb, NO_2 = 50 ppb

Case 1 (referred as the base case) is the original experiment 1141B, the initial conditions for which can be found in Table 2. The simulated results of SOA formation for the seven cases were compared with each other to investigate the impact of NO_x level on SOA formation. Each simulation lasted for six model hours. For each case, the consumed toluene (in units of $\mu g/m^3$) was calculated, and the SOA yield was calculated according to:

$$SOA\ Yield = \frac{Final\ SOA\ Concentration\ at\ end\ of\ Simulation\ (\frac{ug}{m^3})}{Toluene\ Consumption\ (\frac{ug}{m^3})}, \quad (7)$$

Results are shown in Table 11 and Figure10.

Table 11

SOA formation under different NO_x levels.

SOA Concentration (µg/m3)	Base Case NO_x = 0	NO = 50 ppb	NO_2 = 50 ppb	NO = 25 ppb, NO_2 = 25 ppb	NO = 100 ppb	NO_2 = 100 ppb	NO = 50 ppb, NO_2 = 50 ppb
60 min	5.01	6.31	6.30	6.28	5.23	5.38	5.20
120 min	9.72	11.82	11.92	11.84	10.43	10.73	10.49
180 min	14.12	16.61	16.81	16.69	14.92	15.38	15.07
240 min	18.23	20.84	21.14	20.97	18.88	19.49	19.11
300 min	22.04	24.62	24.99	24.78	22.40	23.15	22.71
360 min	25.58	27.99	28.44	28.20	25.55	26.40	25.92
Consumed Toluene (ppm)	3.53E-02	4.76E-02	4.62E-02	4.68E-02	5.11E-02	4.87E-02	4.98E-02
Consumed Toluene (µg/m3)	1.33E+02	1.79E+02	1.74E+02	1.76E+02	1.93E+02	1.83E+02	1.87E+02
SOA Yield	19.26%	15.61%	16.34%	15.98%	13.27%	14.41%	13.83%

It is shown that as NO_x level increases, the total SOA formed from toluene oxidation increases from 25.6 µg/m^3 under zero initial NO_x level to around 28 µg/m^3 under 50 ppb NO_x. However, the SOA yield dropped from 19.26% under zero initial NO_x level to 13.27% under 100 ppb initial NO because of the change in the amount of toluene consumed. Ng et al. (2007) investigated SOA formation from toluene oxidation under low- and high-NO_x levels. Generally, the experimental results and the proposed mechanism in Ng et al. (2007) agrees with this study. SOA yield from toluene photo-oxidation was 36% (higher than in this study) and 10% (lower than this study) under low- and high-NO_x scenarios, respectively. For the low-NO_x case, it is suspected that the SOA yield difference was caused by increased H_2O_2 concentration and the presence of seed aerosols. For the high-NO_x case, NO_x levels approaching 1 ppm were used in the Ng et al. (2007) study. Even though the initial conditions used by Ng et al. (2007) were not exactly the same as the base case in the present study, both studies show similar SOA yield

decreases as NO_x level increases and highlight the importance of reactions of peroxy bicyclic radicals with NO and other peroxy radicals.

Figure 10 also shows that the composition of NO_x also has an impact on SOA yield and formation. NO has a more significant negative impact on SOA yield and formation than NO_2. To investigate the reason for the difference between impacts of NO and NO_2 on SOA formation, constituents of SOA were investigated. The mass fractions of compounds contributing to SOA formation are listed in Table 12.

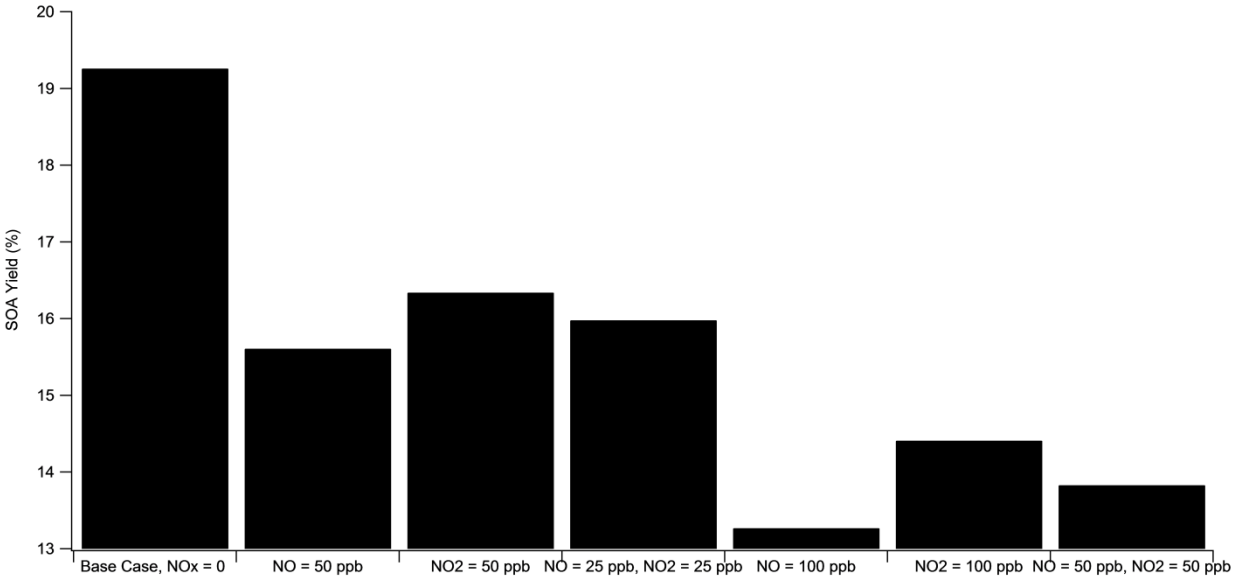

(A)

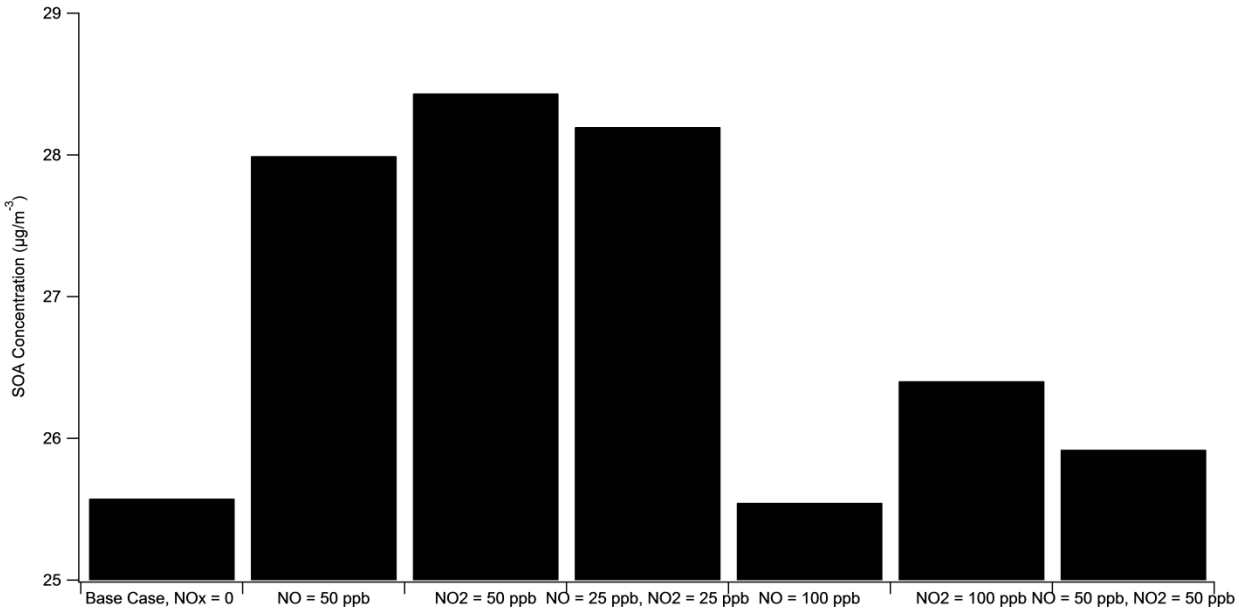

(B)

Fig. 10. Histogram of SOA yields (A) and SOA concentrations (B) under variable NO_x levels.

Table 12

Fractional contribution of compounds to SOA formation for different NO_x levels.

Compound	NO_x = 0	NO = 50 ppb	NO_2 = 50 ppb	NO = 25 ppb, NO_2 = 25 ppb	NO = 100 ppb	NO_2 = 100 ppb	NO = 50 ppb, NO_2 = 50 ppb
AP26		1.3%	1.0%	1.2%	2.5%	1.8%	2.2%
AP27		1.3%	1.0%	1.2%	2.5%	1.8%	2.2%
AP30					1.3%		1.1%
RP42	32.3%	29.4%	30.3%	29.9%	26.6%	28.4%	27.6%
RP45	32.3%	29.4%	30.3%	29.9%	26.6%	28.4%	27.6%
RP48	8.5%	7.7%	7.9%	7.8%	7.0%	7.5%	7.2%
RP50	8.6%	7.9%	8.1%	8.0%	7.1%	7.6%	7.4%
RP53	16.9%	15.4%	15.9%	15.7%	14.0%	14.9%	14.5%
RP54		4.5%	3.0%	3.7%	9.5%	6.1%	7.6%
Total	98.6%	97.1%	97.4%	97.3%	97.1%	96.5%	97.3%

As shown in Table 9, over 98% of SOA in the base case was constituted by bicyclic products from bicyclic peroxy radicals reacting with HO_2. However Figure 3b shows that bicyclic peroxy radicals (take RO_277 in Figure 3b as an example) can react with species other than HO_2 to form different products:

$RO_277 + NO \rightarrow$ AP26 or RAD16 (Reaction 426)

$RO_277 + NO_3 \rightarrow$ RAD16 (Reaction 456)

$RO_277 + RO_2T \rightarrow$ RAD16 or RP40 or RP41 (Reaction 446)

$RO_277 + HO_2 \rightarrow$ RP42 (Reaction 455)

When the NO_x level increases, reaction rates of Reaction 426 and 456 will increase. More RO_277 will be converted into AP26 or RAD16, while less RP42 will be formed due to reduction of available RO_277. This is the reason why AP26 has a larger fraction of SOA and RP 42 has a smaller fraction of SOA as NO_x increases, compared to the base case. With RAD16, β-scission products will be formed, which leads to more RP54. This explains the increase of RP54 fraction when NO_x level increases. However, the increase of SOA formed from AP26 and RP 54 does not compensate for the SOA decrease from the decrease of RP42; thus, SOA yield still decreases as NO_x level increases. The same reasoning is applied to AP27, AP30, RP45, RP48, RP50 and RP53, as well for other bicyclic peroxy radicals. Meanwhile, bicyclic peroxy radicals cannot react with NO_2 directly. NO_2 has be to converted into NO or NO_3 through photochemical reactions and will be able to react with bicyclic peroxy radicals. The gas-phase data for Case 7 (initial NO and NO_2 were both 50 ppb) at the end of the simulation showed that the NO_2 concentration was 250 times larger than that of either NO or NO_3. Therefore, when NO_2 constitutes a large percentage of NO_x, it cannot affect SOA yield directly to as significant an extent.

4. Conclusions

SOA formation from toluene oxidation can be a significant contributor to urban aerosol mass in the atmosphere due to the facts that toluene is one of the most significant contributors to aromatic VOC in the atmosphere (Chan et al., 1991; Na et al., 2005) and that toluene has large SOA yields compared to other VOC (Pandis et al., 1992). To aid in simulating SOA formation from toluene oxidation and understanding the impact of NO_x on its SOA formation, a detailed gas-phase chemical mechanism for toluene oxidation initiated by OH and a gas-aerosol partitioning model have been developed to simulate toluene-related SOA formation.

The gas-phase simulation of toluene, NO_2, and O_3 indicate agreement between experimental data and simulation results as a function of time. The absolute differences between toluene simulated and experimental data were within ±5%, and those for NO_2 and O_3 were within ±15%. Even though the gas-aerosol partitioning model over predicted SOA formation during the first two hours of simulation, the gas-aerosol partitioning model still provided good simulation for SOA formation as a function of time after two hours and good agreement between final experimental and simulated SOA, generally within ±15% difference range. Given the predominance of particles sizes in the atmosphere that are in the hundreds of nanometer size range, it is expected that the model developed here will be applicable to three-dimensional modeling. By tracking toluene oxidation reaction pathways, it was found that more than 98% of SOA mass was contributed by bicyclic products formed from reactions between bicyclic peroxy radicals and HO_2 (RP42, RP45, RP48, RP50, RP53). The fractions of each bicyclic product stayed unchanged as simulation proceeded. Increasing NO_x level causes more bicyclic peroxy radicals to react with NO or NO_3. This resulted in molar yields of more volatile products (such as

AP26) to increase, and molar yields of less volatile products (such as RP42) to decrease. SOA yield decreased as NO_x level increased.

Similar work will be conducted for three additional aromatic hydrocarbons: *m*-xylene, *m*-ethyl-toluene, and 1,2,3-trimethylbenzene. Together with toluene, the four chemicals present two categories of aromatic species: SOA low-yield species (*m*-xylene and 1,2,3-trimethylbenzene) and SOA high-yield species (toluene and *m*-ethyl-toluene) (Odum et al., 1997). Besides the representativeness of the four chemicals, toluene and *m*-xylene are selected due to their presence in surrogate mixtures to develop ozone reactivity scales (Carter, 1995). The resulting updated CACM and an updated partitioning model designed for non-chamber scenarios (Griffin et al., 2003) will be implemented into the California Institute of Technology (CIT) three-dimensional atmospheric chemical transport model for a 1993 smog episode in the South Coast Air Basin of California. With these models, it will be possible to predict more accurately the impact of changing NO_x levels on simulated SOA formation in this very polluted region.

Appendix. Supplementary Data

Molecular structure of chemicals will be attached as supplement.

References

Alvarez, E.G., Viidanoja, J., Munoz, A., Wirtz, K., Hjorth, J., 2007. Experimental confirmation of the dicarbonyl route in the photo-oxidation of toluene and benzene. Environmental Science and Technology 41, 8362-8369.

Atkinson, R., 1990. Gas-phase tropospheric chemistry of organic compounds: a review. Atmospheric Environment 24A, 1-41.

Atkinson, R., Aschmann, S.M., Arey, J., Carter, W.L., 1989. Formation of ring-retaining products from the OH radical-initiated reactions of benzene and toluene. International Journal of Chemical Kinetics 21, 801-827.

Calvert, J.G., Atkinson, R., Becker, K.H., Kamens, R.M., Seinfeld, J.H., Wallington, T.J., Yarwood, G., 2002. The mechanisms of atmospheric oxidation of aromatic hydrocarbons. Oxford University Press, Inc. New York.

Cao, G., Jang, M., 2010. An SOA model for toluene oxidation in the presence of inorganic aerosols. Environmental Science and Technology 44, 727-733.

Carter, W.L., 1990. A detailed mechanism for gas-phase atmospheric reactions of organic compounds. Atmospheric Environment 24A, 481–518.

Carter, W.L., 1995. Development of ozone reactivity scales for volatile organic compounds. Journal of the Air and Waste Management Association 44, 881-899.

Carter,W.L., Cocker III, D.R., Fitz, D.R., Malkinaa, I.L., Bumiller, K., Sauer, C.G., Pisano, J.T., Bufalino, C., Song, C., 2005. A new environmental chamber for evaluation of gas-phase chemical mechanisms and secondary aerosol formation. Atmospheric Environment 39, 7768–7788.

Chan, C.C., Ozkaynak, H., Spengler, J.D., Sheldon, L., 1991. Driver exposure to volatile organic compounds, carbon monoxide, ozone and nitrogen dioxide under different driving conditions. Environmental Science and Technology 25, 964-972.

Charlson, R.J., Schwartz, S.E., Hales, J.M., Cess, R.D., Coakley, JR., J.A., Hansen, J.E., Hofmann, D.J., 1992. Climate forcing by anthropogenic aerosols. Science 24, 423-430.

Chen, J., Griffin, R.J., 2005. Modeling secondary organic aerosol formation from α-pinene, β-pinene, and d-limonene. Atmospheric Environment 39, 7731–7744.

Colville, C.J., Griffin, R.J., 2004a. The roles of individual oxidants in secondary organic aerosol formation from Δ^3-carene 1: gas-phase chemical mechanism. Atmospheric Environment 38, 4001–4012.

Colville, C.J., Griffin, R.J., 2004b. The roles of individual oxidants in secondary organic aerosol formation from Δ^3-carene 2: SOA formation and oxidant contribution. Atmospheric Environment 38, 4013-4023.

Cordes, W., Rarey, J., 2002. A new method for the estimation of the normal boiling point of non-electrolyte organic compounds. Fluid Phase Equilibria 201, 409–433.

Covington, A.K., Dickinson, T. (Eds.), 1973. Physical Chemistry of Organic Solvent Systems. Plenum Press, New York.

Forstner, H.L., Flagan, R.C., Seinfeld, J.H., 1997. Secondary organic aerosol from the photooxidation of aromatic hydrocarbons: molecular composition. Environmental Science and Technology 31, 1345-1358.

Griffin, R.J., Dabdub, D., Seinfeld, J.H., 2002. Secondary organic aerosol-1. atmospheric chemical mechanism for production of molecular constituents. Journal of Geophysical Research 107, 4332-4357.

Griffin, R.J., Nguyen, K., Dabdub, D., Seinfeld, J.H., 2003. A coupled hydrophobic-hydrophilic model for predicting secondary organic aerosol formation. Journal of Physical Chemistry 44, 171-190.

Hildebrandt, L., Donahue, N. M., Pandis, S. N., 2009. High formation of secondary organic aerosol from the photo-oxidation of toluene. Atmospheric Chemistry and Physics 9, 2973-2986.

Hu, D., Tolocka, M., Li, Q., Kamens, R.M., 2007. A kinetic mechanism for predicting secondary organic aerosol formation from toluene oxidation in the presence of NO_x and natural sunlight. Atmospheric Environment 41, 6478-6496.

Jang, M., Kamens, R.M., 2001. Characterization of secondary aerosol from the photooxidation of toluene in the presence of NO_x and 1-propene. Environmental Science and Technology 35, 3626-3639.

Jenkin, M.E., Saunders, S.M., Wagner, V., Pilling, M.J., 2003. Protocol for the development of the master chemical mechanism, MCMv3 (part B): tropospheric degradation of aromatic volatile organic compounds. Atmospheric Chemistry and Physics 3, 181–193.

Jordan, C.E., Ziemann, P.J., Griffin, R.J., Lim, Y.B., Atkinson, R., Arey, J., 2008. Modeling SOA formation from OH reactions with C_8-C_{17} *n*-alkanes. Atmospheric Environment 42, 8015-8026.

Kamens, R.M., Zhang, H., Chen, E.H., Zhou, Y., Parikh, H.M., Wilson, R.L., Galloway, K.E., Rosen, E.P., 2011. Secondary organic aerosol formation from toluene in an atmospheric hydrocarbon mixture: water and particle seed effects. Atmospheric Environment 45, 2324-2334.

Lee, Y.L., Sequeira, R., 1998. Water-soluble aerosol and visibility degradation in Hong Kong during autumn and earlier winter, 1998. Environmental Pollution 116, 225-233.

Myrdal, P.B., Yalkowsky, S.H., 1997. Estimating pure component vapor pressures of complex organic molecules. Industrial and Engineering Chemistry Research 36, 2494–2499.

Na, K., Moon, K., Kim, Y.P., 2005. Source contribution to aromatic VOC concentration and ozone formation potential in the atmosphere of Seoul. Atmospheric Environment 39, 5517-5524.

Nakao, S., Clark, C., Tang, P., Sato, K., Cocker, D., 2011. Secondary organic aerosol formation from phenolic compounds in the absence of NO_x. Atmospheric Chemistry and Physics 11, 10649-10660.

Ng, N.L., Kroll, J.H., Chan, A.W.H., Chhabra, P.S., Flagan, R.C., Seinfeld, J.H., 2007. Secondary organic aerosol formation from m-xylene, toluene, and benzene. Atmospheric Chemistry and Physics Discussions 7, 4085-4126.

Odum, J.R., Hoffmann, T., Bowman, F., Collins, D., Flagan, R.C., Seinfeld, J.H., 1996. Gas/particle partitioningand secondary organic aerosol yields. Environmental Science and Technology 30, 2580–2585.

Odum, J.R., Jungkamp, T.P.W., Griffin, R.J., Flagan, R.C., Seinfeld, J.H., 1997. The atmospheric aerosol-forming potential of whole gasoline vapor. Science 276, 96-99.

Pandis, S.N., Harley, R.A., Cass, G.R., Seinfeld, J.H., 1992. Secondary organic aerosol formation and transport. Atmospheric Environment 26, 3369-2282.

Pankow, J.F., 1994a. An absorption model of the gas/aerosol partitioning of organic compounds in the atmosphere. Atmospheric Environment 28, 185–188.

Pankow, J.F., 1994b. An absorption model of the gas/aerosol partitioning involved in the formation of secondary organic aerosol. Atmospheric Environment 28, 189–193.

Sato, K., Hatakeyama, S., Imamura, T., 2007. Secondary organic aerosol formation during the photooxidation of toluene: NO_x dependence of chemical composition. The Journal of Physical Chemistry 2007, 9796-9808.

Saunders, S.M., Jenkin, M.E., Derwent, R.G., Pilling, M.J., 2003. Protocol for the development of the master chemical mechanism, MCMv3 (part A): tropospheric degradation of non-aromatic volatile organic compounds. Atmospheric Chemistry and Physics 3, 161–180.

Schwartz, J., Neas, L.M., 2000. Fine particles are more strongly associated than coarse particles with acute respiratory health effects in schoolchildren. Epidemiology 11, 6-10.

Stroud, C.A., Makar, P.A., Michelangeli, D.A.,Mozurkewich, M., Hastie, D.R., Barbu, A., Humble J., 2004. Simulating organic aerosol formation during the photooxidation of toluene/NO_x mixtures: comparing the equilibrium and kinetic Assumption. Environmental Science and Technology 38, 1471-1479.

Suh, I., Zhang, D., Zhang, R., Molina, L.T., Molina, M.J., 2002. Theoretical study of OH addition reaction to toluene. Chemical Physics Letters 364, 454–462.

Suh, I., Zhang, R., Molina, L.T., Molina, M.J., 2003. Oxidation mechanism of aromatic peroxy and bicyclic radicals from OH-toluene reactions. Journals - American Chemical Society 125, 12655-12665.

Volkamer, R., Jimenez, J.L., Martini, F.S., Dzepina, K., Zhang, Q., Salcedo, D., Molina, L.T., Worsnop, D.R., Molina, M.J., 2006. Secondary organic aerosol formation from anthropogenic air pollution: rapid and higher than expected. Geophysical Research Letters 33, 17811-17814.

Volkamer, R., Ziemann, P.J., Molina, M.J., 2009. Secondary organic aerosol formation from acetylene (C_2H_2): seed effect on SOA yields due to organic photochemistry in the aerosol aqueous phase. Atmospheric Chemistry and Physics 9, 1907-1928.

Whitten, G.Z., Heo, G., Kimura, Y., McDonald-Buller, E., Allen, D.T., Carter, W.L., Yarwood, G., 2010. A new condensed toluene mechanism for carbon bond: CB-5-TU. Atmospheric Environment 44, 5346-5355.

Appendix

Supplementary Table 1.

Molecular structures of chemicals.

Chemical	Molecular Structure
AP25	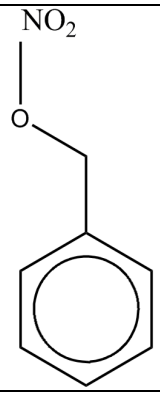
AP26	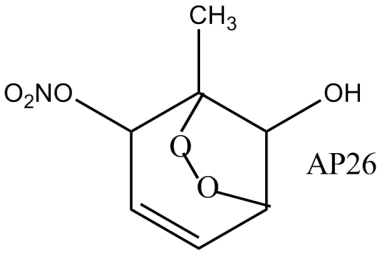
AP27	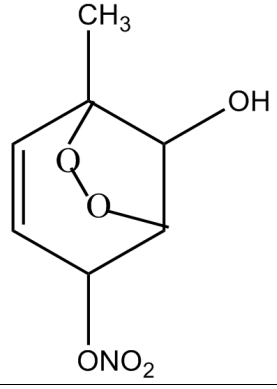

AP28	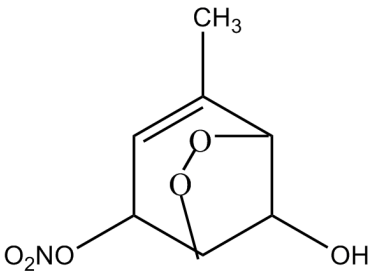
AP29	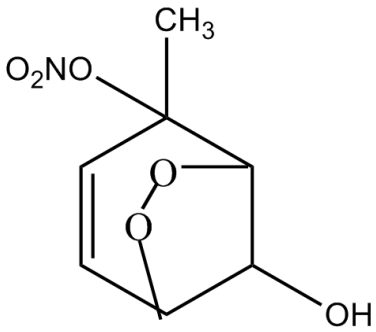
AP30	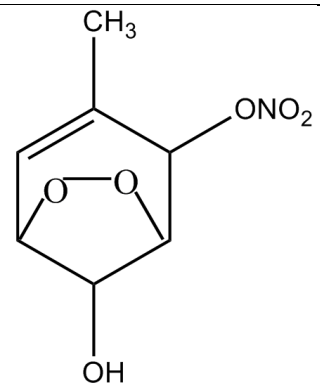
RAD9	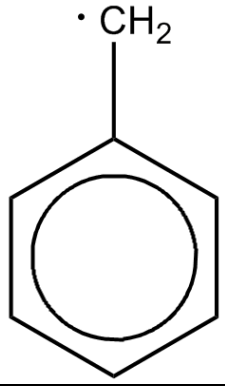

RAD10	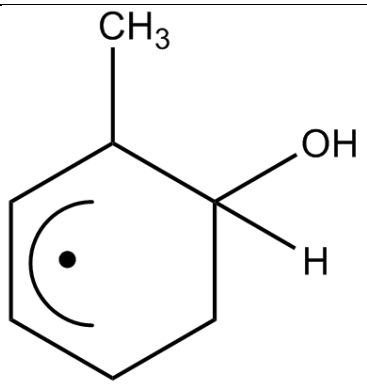
RAD11	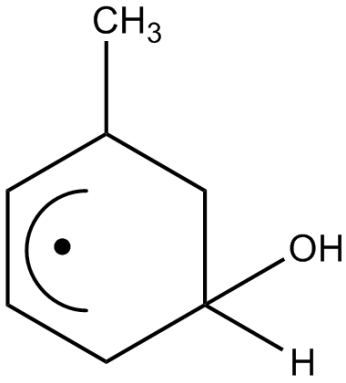
RAD12	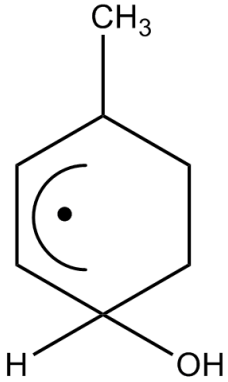
RAD13	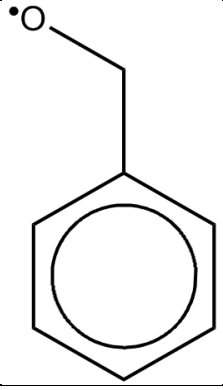

RAD14	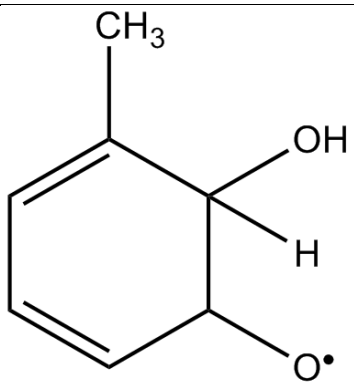
RAD15	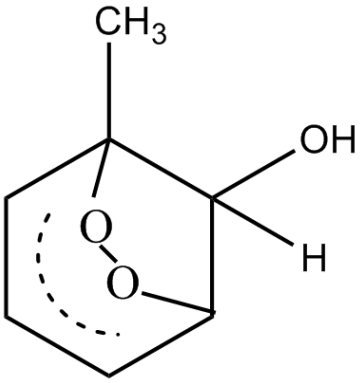
RAD16	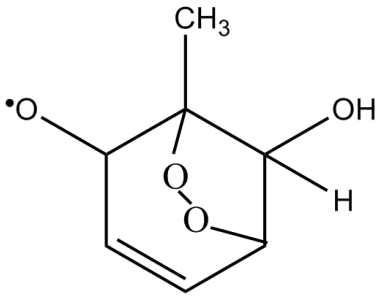
RAD17	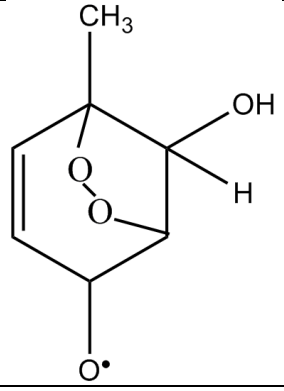

RO275	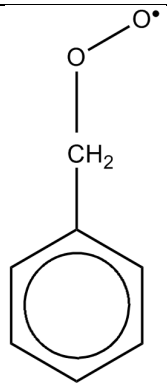
RO276	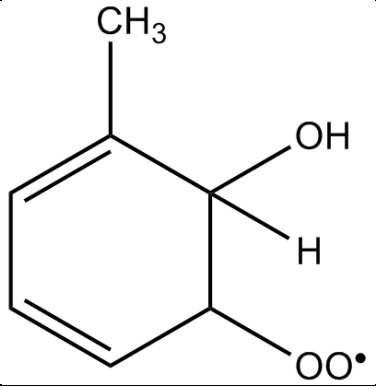
RO77	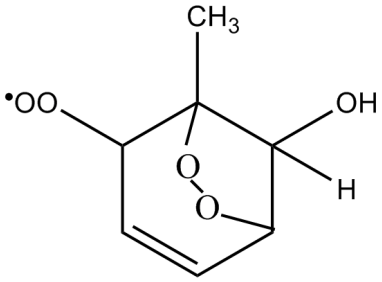
RO78	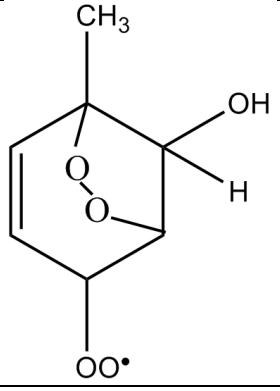

RP24	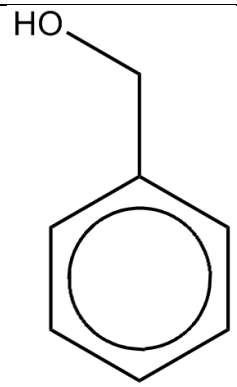
RP25	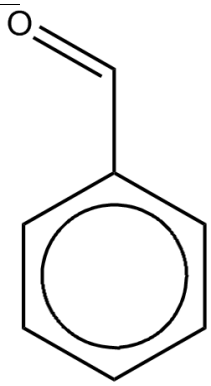
RP26	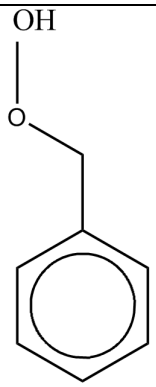
RP27	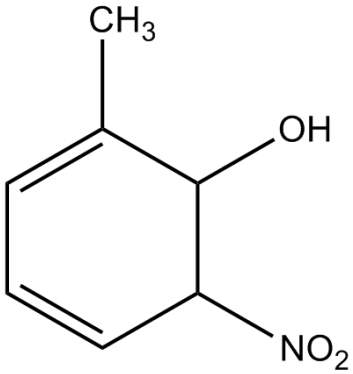

RP28	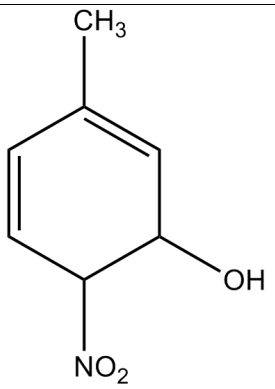
RP29	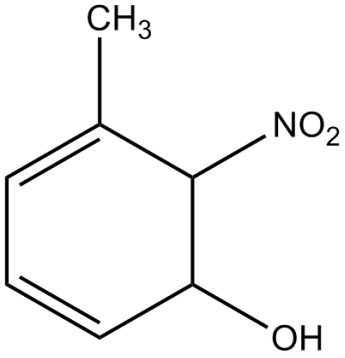
RP30	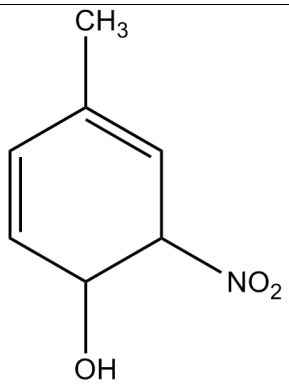
RP31	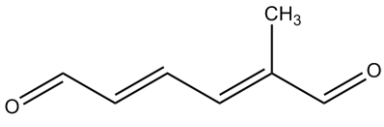

RP32	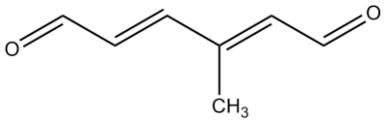
RP33	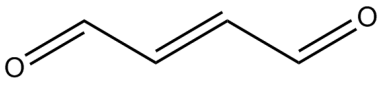
RP34	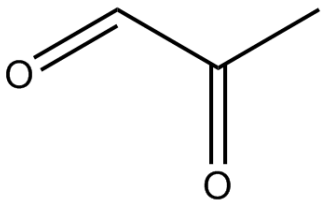
RP35	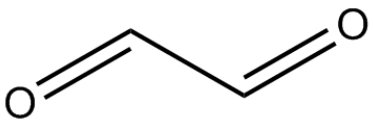

RP36	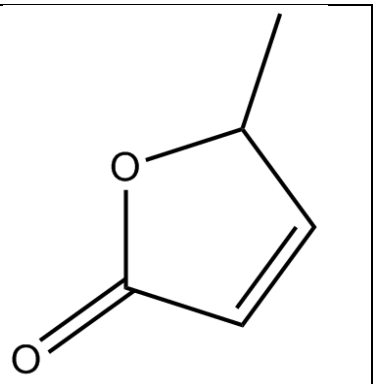
RP37	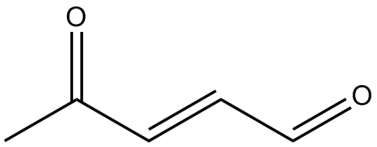
RP38	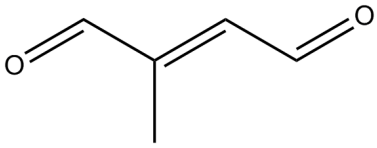
RP39	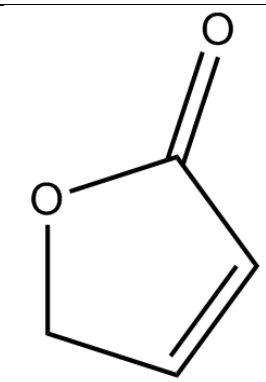

RP40	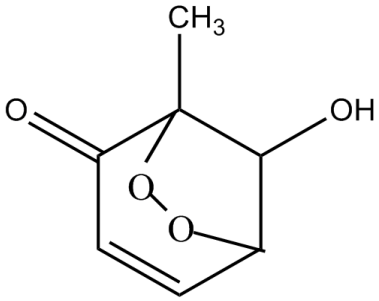
RP41	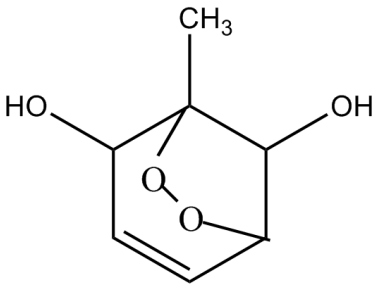
RP42	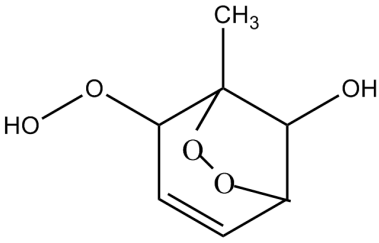
RP43	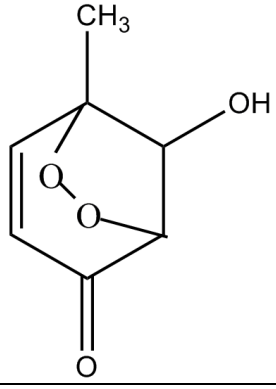

RP44	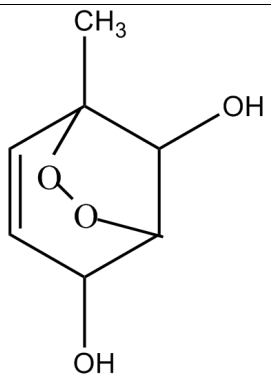
RP45	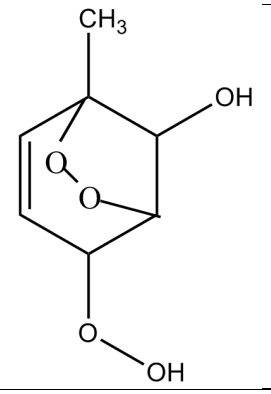
RP46	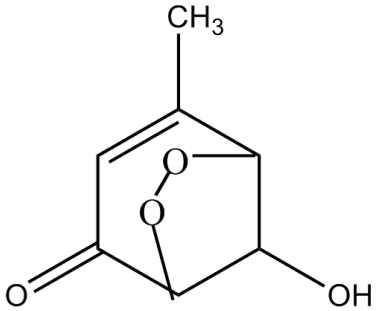
RP47	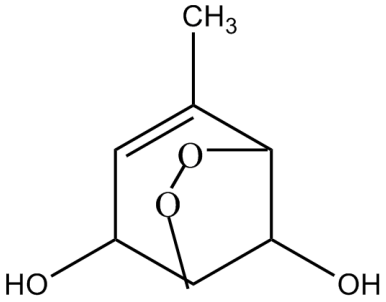

RP48	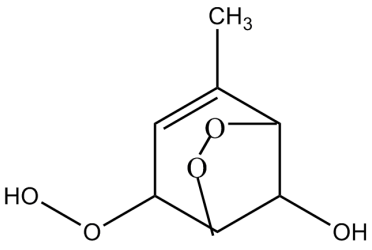
RP49	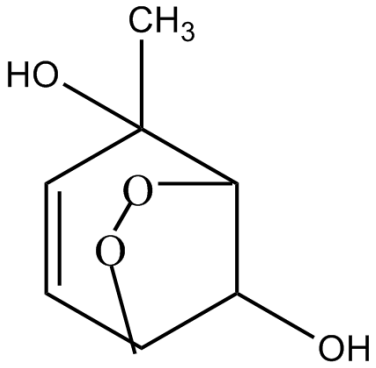
RP50	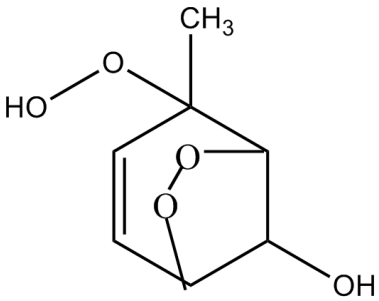
RP51	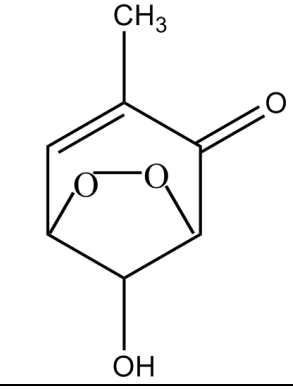

RP52	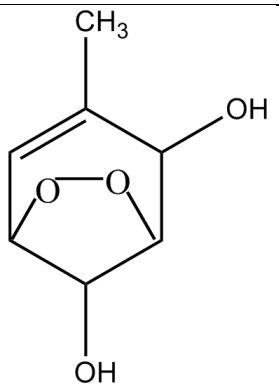
RP53	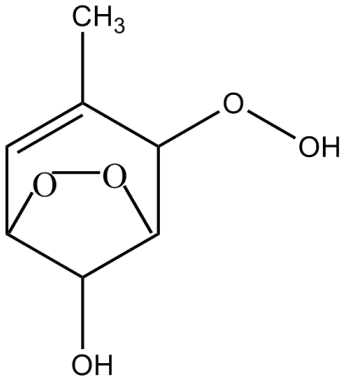
TOLU	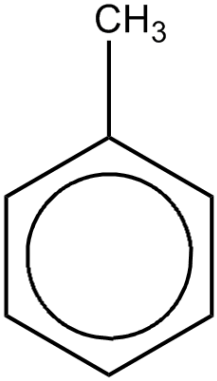
UR52	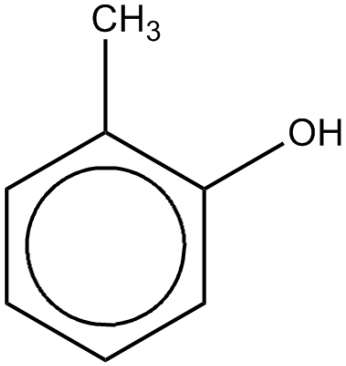

UR53	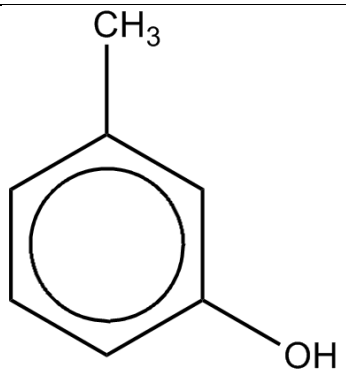
UR54	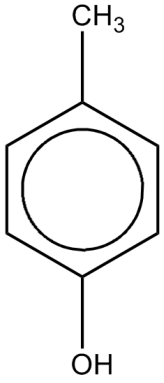
UR55	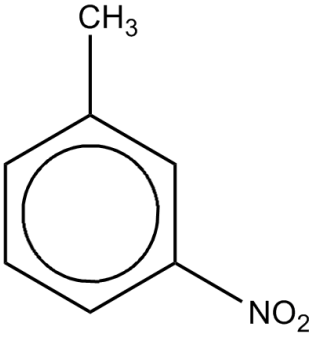
UR56	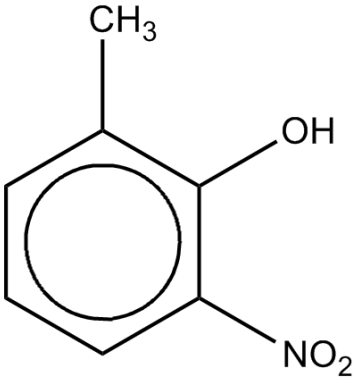

UR57	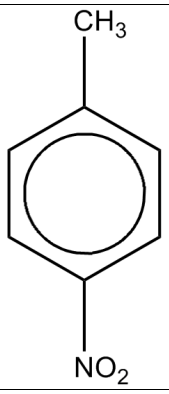
UR58	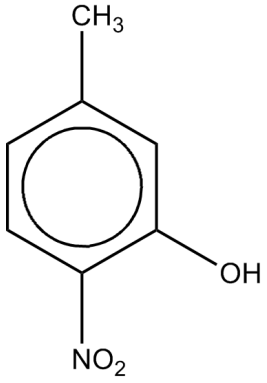
UR59	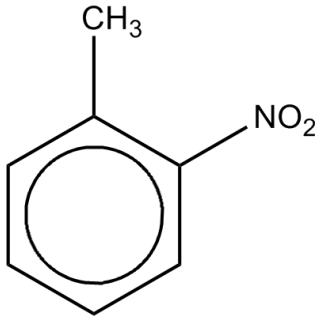
UR60	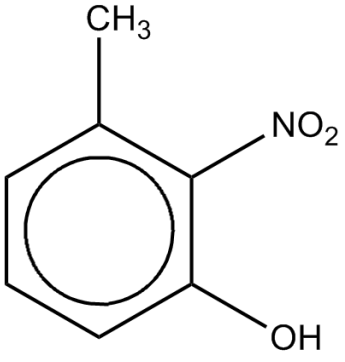

UR61	Same as UR55
UR62	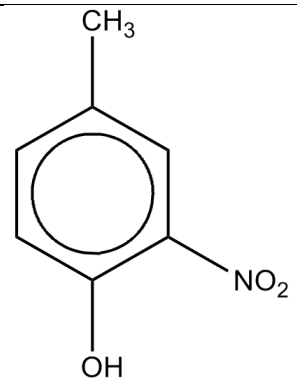
UR63	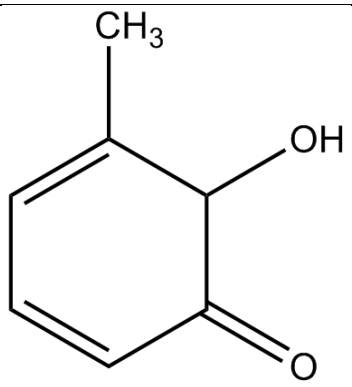
UR64	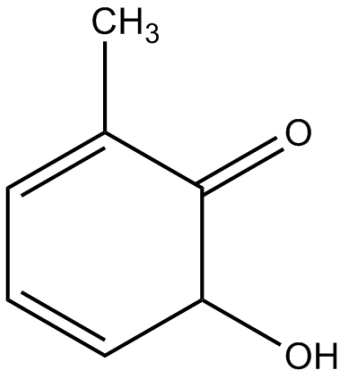

UR65